

Hydrogen production by water splitting using gas switching technology

Journal Article

Author(s):

Ugwu, Ambrose; Donat, Felix; Zaabout, Abdelghafour; Müller, Christoph; Albertsen, Knuth; Cloete, Schalk; van Diest, Geert; Amini, Shahriar

Publication date:

2020-06-15

Permanent link:

<https://doi.org/10.3929/ethz-b-000416994>

Rights / license:

[Creative Commons Attribution 4.0 International](#)

Originally published in:

Powder Technology 370, <https://doi.org/10.1016/j.powtec.2020.05.039>



Hydrogen production by water splitting using gas switching technology

Ambrose Ugwu^{a,**}, Felix Donat^b, Abdelghafour Zaabout^c, Christoph Müller^b, Knuth Albertsen^d, Schalk Cloete^c, Geert van Diest^d, Shahriar Amini^{a,c,*}

^a Norwegian University of Science and Technology, Norway

^b Laboratory of Energy Science and Engineering, ETH, Zürich, Switzerland

^c SINTEF Industry, Trondheim, Norway

^d Euro Support Advanced Materials B.V., The Netherlands

ARTICLE INFO

Article history:

Received 5 September 2019

Received in revised form 13 March 2020

Accepted 12 May 2020

Available online 15 May 2020

Keywords:

Gas switching

Hydrogen production

Chemical looping

Carbon capture

Zero-emission

Production

Fluidization

Oxygen carrier

Water

Splitting

Watersplitting

Iron

Natural gas

cGHG

Climate change

ABSTRACT

This study demonstrates a novel “Gas Switching Water Splitting (GSWS)” technology for production of pure H₂ with integrated CO₂ capture. The reactor concept is based on the chemical looping technology where an oxygen carrier (metal oxide) is used to transport O₂ from air to the fuel for different redox reactions. Unlike the conventional chemical looping, Gas Switching Technology inherently avoids external circulation of the oxygen carrier by alternating the oxidizing and reducing gases in a single bubbling fluidized bed reactor. This greatly simplifies reactor design leading to easier scale-up of the technology in comparison with the conventional chemical looping. The first experimental demonstration of the GSWS concept was completed at atmospheric pressure and temperatures ranging between 700 °C and 900 °C with iron-based oxygen carrier supported on alumina (~35 wt% Fe₂O₃ on Al₂O₃). Approximately 99% H₂ purity was achieved at ~80% oxygen utilization. Significant fuel slippage was observed especially beyond 33% degree of reduction with some carbon deposition. The deposited carbon was able to combust/gasify completely in the subsequent air stage which makes the concept robust in sustaining oxygen carrier life. However, the gas mixing between the GSWS stages reduced the H₂ purity, CO₂ purity, and CO₂ capture efficiency. To minimize the negative impact of gas mixing, Cu doped Mg(Fe_{0.9}Al_{0.1})₂O₄ spinel with 74 wt% active content was developed specifically for the second experimental demonstration. Despite the high stability and reactivity under redox conditions with TGA, this oxygen carrier did not perform optimally in 5 cm ID fluidized bed reactor because of excessive agglomeration at degree of reduction beyond 34%. In general, a range of the active content between 35 and 70 wt% of the oxygen carrier was desired for optimal performance of the GSWS concept.

© 2020 The Authors. Published by Elsevier B.V. This is an open access article under the CC BY license (<http://creativecommons.org/licenses/by/4.0/>).

1. Introduction

The Intergovernmental Panel on Climate Change (IPCC) has predicted that the global average temperature would increase between 3.7 and 4.8 °C by 2100 above pre-industrial levels if no actions were taken to reduce anthropogenic CO₂ emissions [1]. According to the Paris climate target, these emissions must reduce by approximately 45% from 2010 levels by 2030, reaching net zero in 2050 in order to keep the global temperature rise below 1.5 °C [2] (or by ~25% by 2030 and reach net zero in 2070 in the 2 °C temperature rise scenario). Despite the urgent warning to reduce greenhouse gas (GHG) emission, CO₂ emission has continued to increase due to the rise in global energy demand and high reliance on fossil fuel [3–5]. This situation is critical

with current signs of adverse signs of climate change from the excessive heat waves, wild fire, among others. For the Paris climate agreement target to be achieved to save our planet, it is crucial to switch more towards clean energy carriers such as H₂ in the energy mix [6,7]. H₂ is considered a clean energy carrier for the future since the combustion is associated with no CO₂ emission and it could be produced from a range of primary energy sources [8] (water, hydrocarbons, and other organic matter). As a secondary energy source, the environmental impact of hydrogen depends greatly on these primary sources and the production process [9]. The major challenge is the ability to extract H₂ economically and efficiently from these primary sources with minimum CO₂ emissions [8–10].

Currently, H₂ is mainly produced at large scale through the steam reforming of natural gas but associated with significant CO₂ emissions as the heat required for the highly endothermic reforming is provided by the combustion of fossil fuel outside the reforming reactor [11]. To address this concern, two main zero-emission technologies have been identified for H₂ production [9]: i) the conversion of fossil fuel with

* Corresponding author at: Norwegian University of Science and Technology, Norway.

** Corresponding author.

E-mail addresses: ambrose.ugwu@ntnu.no (A. Ugwu), shahriar.amini@sintef.no (S. Amini).

Nomenclature

Abbreviations

BET	Brunauer Emmett Teller
CCS	Carbon capture and storage
CFB	Circulation Fluidized Bed
CLC	Chemical Looping Combustion
CLR	Chemical Looping Reforming
EDS	Energy Dispersive Spectroscopy
EDX	Energy Dispersive X-Ray Spectroscopy
GHG	Gashouse Gas
GSC	Gas Switching Combustion
GST	Gas Switching Technology
GSWS	Gas Switching Water Splitting
ICP-OES	Inductively coupled plasma optical emission spectroscopy
OC	Oxygen carrier
POX	Partial Oxidation of Methane
SEM	Scanning Electron Microscopy
TEM	Transmission Electron Microscopy
XRD	X-ray Diffraction
TGA	Thermogravimetric Analysis

Symbols

C_{dep}	Carbon deposition
D_{50}	Diameter of the catalyst which 50% of a sample mass is smaller than
n_{CO}	Mole of CO at the gas outlet
n_{CO_2}	Mole of CO ₂ at the gas outlet
$n_{CO_2,air}$	Mole of CO ₂ in the outlet gas at the air stage
$n_{CO_2,fuel}$	Mole of CO ₂ in the outlet gas at the fuel stage
$n_{CO_2,steam}$	Mole of CO ₂ in the outlet gas at the steam stage
$n_{fuel,in}$	Mole of fuel input
$n_{fuel,out}$	Mole of fuel at the gas outlet
$n_{Fe_2O_3}$	Mole of Fe ₂ O ₃
n_{H_2}	Mole of H ₂ at the gas outlet
n_{H_2O}	Mole of H ₂ O at the gas outlet
n_{N_2}	Mole of N ₂ at the gas outlet
n_{O_2}	Mole of O ₂ at the gas outlet
S_{CO_2}	CO ₂ selectivity
η_{CO_2}	CO ₂ capture efficiency
σ_{H_2}	H ₂ purity
σ_{CO_2}	CO ₂ purity
γ_{fuel}	Fuel conversion
γ_{H_2O}	Steam conversion

integrated CO₂ capture [12] and ii) the utilization of carbon-free sources such as the electrolysis of water using renewable electricity such as solar, wind, etc. [13]. It is worth mentioning that the energy penalty and cost of these technologies should be competitive compared to other options in order to make them commercially viable [13,14]. Chemical looping with inherent CO₂ capture has been demonstrated as a technology capable of addressing the high energy penalty and cost relative to other carbon capture and storage (CCS) technologies [12,15,16]. This made chemical looping an attractive technology to be extended to energy-intensive processes such as H₂ production [15–20]. Chemical looping process for H₂ production was introduced by Howard Lane and his co-workers as a steam-iron process in 1903 [9,21,22]. This process has been demonstrated at lab and pilot scales under atmospheric conditions [23–32].

However, high-pressure operation of these chemical looping concepts is necessary for maximizing the energy efficiency and competitiveness with other H₂ production technologies [33]. To date, only a few studies on pressurized chemical looping in an interconnected

fluidized bed configuration have been completed [34–37], despite the predicted benefits of such technology in terms of increased energy efficiency [38]. A major challenge is the difficulty to scale up under pressurized conditions, due to the high complexity and the need for precise circulation of large quantities of oxygen carrier material between different interconnected reactors as shown in Fig. 1 (a & b) given that each reactor vessel should be pressurized independently while it is essential to fulfilling the heat and mass balance. In this situation, any instantaneous pressure imbalance between the reactors may induce instabilities in solids circulation, which could, in turn, result in large leakages through the sealing devices. This would reduce the CO₂ purity and capture efficiency and increases explosion risks if unreacted fuel gas mixes with the air. Also, the stress imposed on the material through solid circulation could change the morphology of the oxygen carrier thereby reducing the lifetime through excessive fragmentation.

Attempts have been made in recent years to address these issues through novel reactor concepts with no external solid circulation including gas switching in a packed bed reactor [41,42], gas switching in a fluidized bed reactor [40,43–47] and internal circulating reactor [48], but the focus of this work is on gas-switching fluidized bed reactors. Unlike the conventional chemical looping, this novel technology utilizes a single fluidized bed reactor and avoids the circulation of oxygen carrier by alternating the feeds of the oxidizing and reducing gases to depict different redox stages as shown in Fig. 1 b. With this arrangement, a wide range of inlet flow rates can be accommodated and scale-up challenges can be greatly reduced. Experimental studies have proven that this concept works under atmospheric and high-pressure conditions showing ease of operation and control [49–51]. Gas Switching Technology (GST) has also been proposed for combustion for power generation [52,53], H₂ production through methane reforming [43,44,46,49,50], GHG (CO₂ and CH₄) utilization through dry reforming [47] and in some cases provide flexibility in terms of product (H₂ or power) [54].

To capitalize on this success, this study extends the GST to the water splitting using the steam-iron process for efficient H₂ production. Fig. 2 presents a schematic reactor arrangement of a conventional chemical looping technology for H₂ production through water splitting and the gas-switching alternative. The water splitting is a three-step process utilizing the different iron oxide states to produce H₂ with integrated CO₂ capture. In the first stage, Fe₂O₃ is reduced to FeO/Fe using a gaseous fuel (CH₄, CO, syngas, etc). This is followed by the 2nd stage where steam is supplied for the partial oxidation (slightly exothermic) of the FeO/Fe to produce Fe₃O₄ and pure H₂. Air is supplied at the 3rd stage to fully oxidize back the oxygen carrier to Fe₂O₃. This last step (oxidation) is also used to regenerate the oxygen carrier and produce heat for the process.

Following the looping route (Fig. 2 a) for this purpose requires a complex set-up of three interconnected reactors with the circulation of solid oxygen carrier to fulfill both the heat and mass balance requirements [3,55,56] whereas the gas switching approach (Fig. 2 b) requires only one fluidized bed reactor with gas feeds alternated in-between stages to achieve the redox reaction without solid circulation.

Since the reactions all happen in a single reactor vessel, this new reactor concept enables easy and more effective utilization of heat of reactions to reduce the energy penalty of the process. The reduction of the oxygen carrier (Fe₂O₃ to FeO/Fe) with CH₄ is endothermic and is thermodynamically more favored at high temperature [3] whereas the oxidation of FeO to Fe₃O₄ with steam is slightly exothermic thus the reaction is more favored at low temperature.



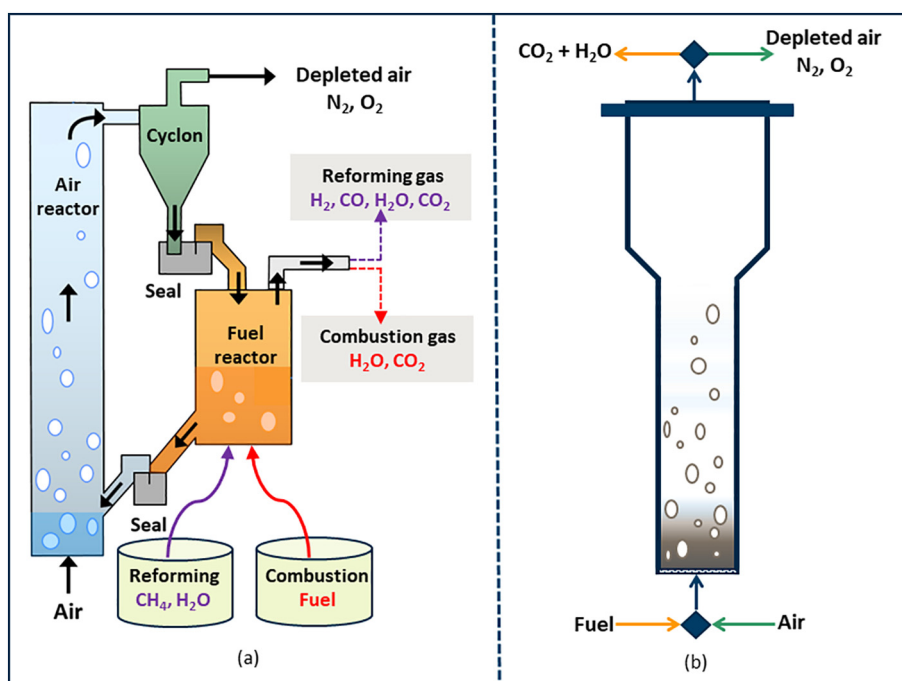


Fig. 1. Chemical looping and Gas Switching Technology for reforming and combustion applications. A) represents a scheme of conventional chemical looping reforming and combustion [39] while b) represents the simplified Gas Switching configuration of Chemical Looping Combustion [39].



A conceptual disadvantage that GSWS has over the three-reactor process, is the mixing of gases when switching from one reaction stage to another, affecting CO₂ capture efficiency, CO₂ purity, and H₂ purity. The extent of the gas mixing depends on the flow rates and volume of the reaction vessel. It is therefore important that the fuel and steam stages are long enough to minimize the extent of the mixing of different gases in the system to achieve an acceptable capture efficiency and product gas purity. Fig. 3 shows the separation performance against the redox-active content of the oxygen carrier computed using the mass balance at 20 bar and 800 °C assuming a perfectly mixed reactor. The H₂ purity, CO₂ purity and CO₂ capture efficiency are quantified in section 2.2.1 (Eq. 11 – Eq. 13) respectively. 80% oxygen carrier utilization was assumed to achieve a degree of reduction from Fe₂O₃ to FeO using

CH₄ as fuel. The assumption to limit the degree of reduction only to FeO was considered because further reduction would i) lead to substantial fuel slip due to equilibrium limitations, ii) cause particle agglomeration and iii) lead to excessive coking. Clearly, CO₂ capture, CO₂ purity and H₂ purity increase substantially with increasing the oxygen carrier active content (Fe₂O₃). Oxygen carrier with higher active content would facilitate longer fuel, steam and air stages, thereby reducing the impact of the undesired mixing when a high-pressure operation is targeted.

In summary, this work demonstrates the experimental operation of the water-splitting process for pure H₂ production which could be coupled with other downstream chemical process using the Gas Switching configuration. It explicitly highlights the advantages and disadvantages of this configuration in terms of oxygen carrier selection and development, cycle design, and reactor performance (fuel and steam

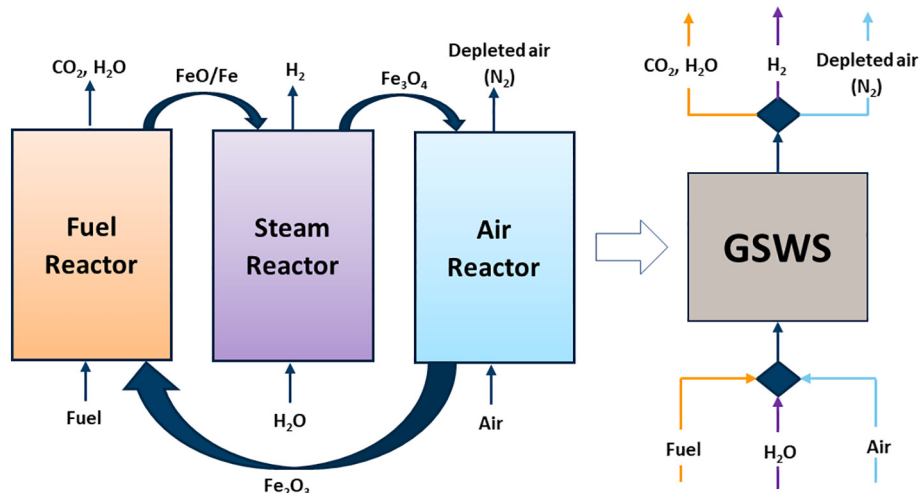


Fig. 2. a: Water-splitting process completed following the conventional chemical looping route. b: Configuration of a simplified Gas Switching Water Splitting, GSWS.

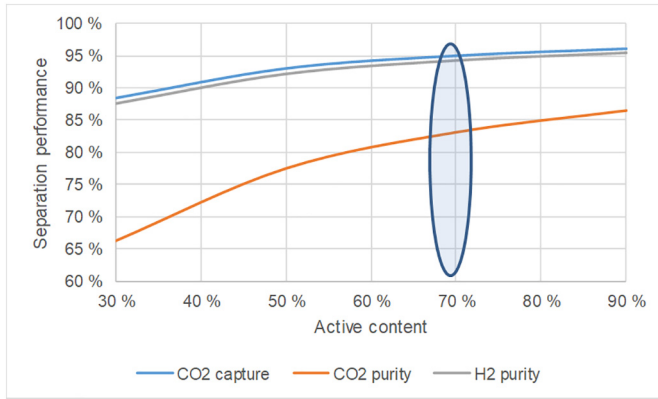


Fig. 3. The separation performance at 20 bar and 800 °C assuming 80% degree of reduction from Fe_2O_3 to FeO .

conversion, carbon deposition, CO_2 and H_2 purity, CO_2 capture efficiency, oxygen carrier, agglomeration, etc.).

2. Experiments and methods

2.1. Experimental setup

The GSWS experiment was completed using a lab-scale fluidized bed reactor (Fig. 4). A fluidized bed is desired to achieve good mixing to minimize concentration and temperature variation in the bed

[57–59]. This reactor consists of a cylindrical column (5 cm in inner diameter and 50 cm in height) and a freeboard zone consisting of an expanding conic zone (5 cm in the lower end diameter, 10 cm at the top end diameter and 40 cm height) to minimize particles elutriation. The reactor is made of Inconel 600 with the capability of withstanding high-temperature gas-solids reactive flows (up to 1000 °C). A porous plate distributor made of Inconel 600 with 20 μm mean pore size and 3 mm thickness was used to ensure good gas distribution. The reactor vessel is heated up to a target temperature using an external electrical heating element wound around the reactor. The reactor was also insulated using a 25 cm thick blanket insulation to prevent excessive heat loss. Automatic gas switching and feed into the reactor were achieved using a three-way electrical automatic switching valve and mass flow controllers from Bronkhorst BV respectively. A cooler was installed at the outlet of the reactor to cool down the stream of hot gases before being sent to the gas analyzer and to the vent. The gas composition was measured using a syngas analyzer (ETG Risor e Tecnologia) while the bed temperature was measured using two thermocouples inserted at 2 and 20 cm above the gas distributor respectively. A LabVIEW application was used for data acquisition/storage and to control all the measurement instruments and devices.

2.1.1. Thermogravimetric analyzer

The cyclic performance of the oxygen carrier was evaluated in a thermogravimetric analyzer (Mettler Toledo, TGA/DSC 1) at atmospheric pressure. The sample was loaded in a 30 μl alumina crucible that sat on the crucible holder attached to the balance beam and was heated to the desired temperature (usually 850 °C) under a reactive gas flow of 125 mL min^{-1} air, measured at normal temperature and pressure,

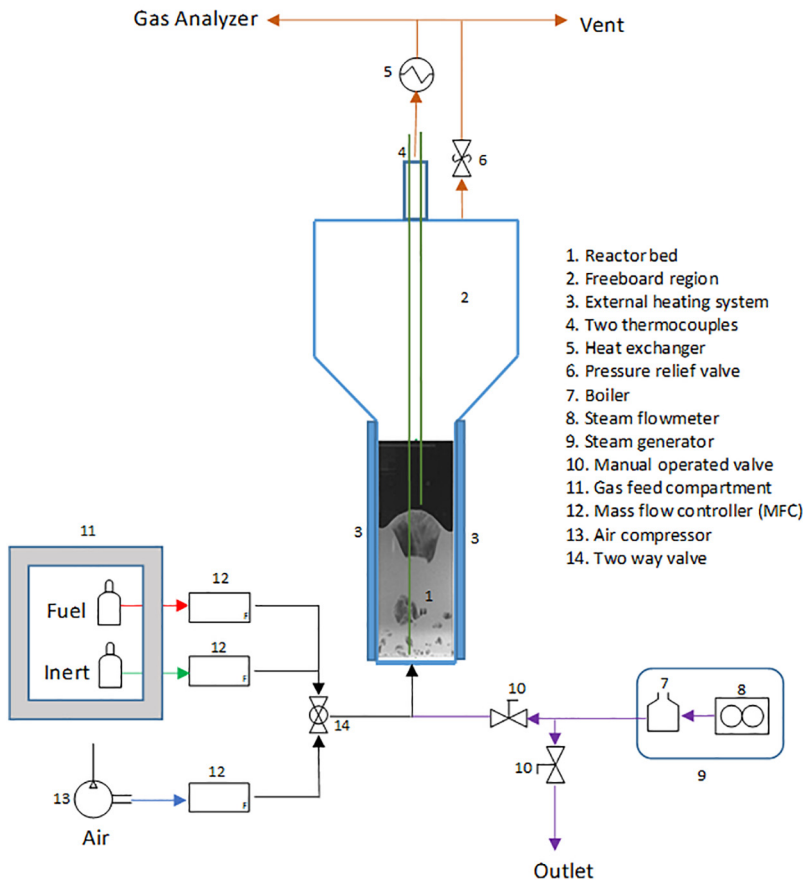


Fig. 4. The experimental setup [43,44,47] used for GSWS demonstration tests . a) schematic diagram, b) the actual reactor setup.

NTP. In addition, a purge gas flow of $25 \text{ mL min}^{-1} \text{ N}_2$ was present throughout the experiment. The reactant gases were supplied through a fine capillary mounted on the cantilever arm terminating just above, and before, the crucible, which means that the measured rate of mass change was largely governed by diffusion in vertical direction from the bulk of the gas to the surface of the sample inside the alumina crucible (note that the gas flowed horizontally over the alumina crucible containing the sample). When the set temperature was reached, the cycling experiment started: The reduction step (25 min) was performed using 6.7 vol% CH_4 in N_2 , followed by a purge step (2 min) and the oxidation step (11 min) using air. Sixty redox cycles were typically carried out. In some experiments, an additional oxidation step was performed using 20 vol% CO_2 in N_2 (prior to the air oxidation step).

2.1.2. X-ray diffraction

Powder XRD (PANalytical Empyrean) was used to investigate the chemical composition of the crystalline phases of the as-synthesized and cycled oxygen carriers. The diffractometer was operated at 45 kV and 40 mA using $\text{CuK}\alpha$ radiation and each sample was scanned over the range of $2\theta = 10\text{--}90^\circ$ with a step size of 0.0167° . The total time for each measurement was 1 h.

For in-situ measurements, the diffractometer was equipped with an Anton Paar XRD 900 high-temperature reactor chamber where the sample was placed onto a glass-ceramic disc made of Macor and exposed to different gas atmospheres at 850°C . For each atmosphere, multiple measurements were made to track the evolution of crystalline phases over the range $2\theta = 20\text{--}80^\circ$ with a step size of 0.0167° ; each measurement thus lasted 12 min. First, the sample was reduced in 4.4 vol% CH_4 in N_2 (30 measurements), then re-oxidized in 15 vol% CO_2 in N_2 (15 measurements) and finally oxidized in 50 vol% air in N_2 (5 measurements). The cell was purged with pure N_2 for 2 min between the reaction stages. The total flow rate of gas was kept constant at 200 mL min^{-1} (at NTP) and was controlled by a set of mass flow controllers (Bronkhorst, EL-FLOW series) synchronized with the diffractometer and the temperature controller of the high-temperature reaction chamber.

2.1.3. Inductively coupled plasma optical emission spectroscopy (ICP-OES)

The molar ratio of Mg:Fe:Al:Cu in the oxygen carrier was determined via ICP-OES using an Agilent 5100 VDV. Matrix effects were lessened by matching the matrix acids for all blanks, standards (multielement standard) and samples.

2.1.4. Scanning electron microscopy

A scanning electron microscope (FEI Quanta 200 FEG) operated at 10 kV was used to characterize the surface morphology of the materials. A double-sided carbon tape was used to attach samples onto an aluminum holder. Prior to SE imaging, the samples were sputter coated (Safematic CCU-010) with an $\sim 5 \text{ nm}$ -thick layer of PtPd. Transmission electron microscopy (TEM) images of as-synthesized samples were obtained using a FEI Talos F200X microscope operated at 200 kV, equipped with a high-brightness Schottky field-emission gun (FEG), a high-angle annular dark field (HAADF) detector and a large collection-angle energy-dispersive X-ray spectroscopy (EDX) detector.

2.1.5. Crushing strength

The crushing strength of the oxygen carrier (as-synthesized and after $>40 \text{ h}$ of redox operation in the TGA) was obtained by measuring the force required to break individual oxygen carrier particles sieved to $180\text{--}212 \mu\text{m}$ using a force gauge operated at 50 Hz (Shimpo, FGN-20). The crushing strength was defined as the first local maximum in the recorded data when compressing the particle. At least 40 such measurements were performed to give meaningful results.

2.2. Methodology

The gas switching water splitting (GSWS) was demonstrated using an iron-based oxygen carrier with the reactor configuration as shown in Fig. 2 b in a fluidized bed reactor (Fig. 4). A three-stage cycle (fuel, steam and air stage) was designed to complete the GSWS process. The cycle starts with the fuel stage where the oxygen carrier is reduced to FeO or Fe using dry fuel (CO or CH_4) with inherent separation of CO_2 . The steam stage follows immediately after the fuel stage where steam is fed to partially oxidize FeO/Fe to Fe_3O_4 while producing H_2 . The final stage of the GSWS cycle is the air stage for complete oxidation of Fe_3O_4 to Fe_2O_3 associated with heat generation as explain in the introduction (Section 1). For each reaction condition, real-time temperature, pressure and gas composition were recorded and analyzed. The separation performance was also evaluated through mass balance with the following indicators: CO_2 purity, H_2 purity, and CO_2 capture efficiency as also described in section 2.2.1. To avoid carbon deposition, the extent of reduction was limited to FeO, although this reduced H_2 yield substantially in line with thermodynamics.

2.2.1. Reactor performance measures

The objective of the GSWS process is to convert a hydrocarbon fuel to H_2 . Thus, it is desired to maximize the fuel conversion in the fuel stage and maximize H_2 production in the steam stage. From this point of view, the following performance measures have been defined for quantifying the reactor performance. Note that n_i specifies the total moles of species i exiting the reactor during a given stage unless specifically indicated for the moles entering the reactor as $n_{i, \text{in}}$. Firstly, the fuel conversion in the fuel stage is quantified as follows:

$$\gamma_{\text{fuel}} = \frac{n_{\text{fuel, in}} - n_{\text{fuel, out}}}{n_{\text{fuel, in}}} \quad (6)$$

However, conversion of CH_4 to achieve partial oxidation achieves four times less oxygen carrier reduction than the conversion of CH_4 to achieve full oxidation. Thus, the selectivity of CH_4 conversion to CO_2 is also quantified.

$$s_{\text{CO}_2} = \frac{n_{\text{CO}_2}}{n_{\text{CO}} + n_{\text{CO}_2}} \quad (7)$$

One of the goals of the fuel stage is to maximize the degree of oxygen carrier utilization. This parameter is quantified as follows, assuming that oxygen carrier reduction is carried out from Fe_2O_3 to FeO:

$$X_{\text{red}} = \frac{\text{oxygen transferred to fuel}}{\text{oxygen available}} = \frac{n_{\text{CO}} + 2n_{\text{CO}_2} + n_{\text{H}_2\text{O}}}{3n_{\text{Fe}_2\text{O}_3}} \quad (8)$$

When looking at the steam stage, the primary performance measure is the degree of steam conversion:

$$\gamma_{\text{H}_2\text{O}} = \frac{n_{\text{H}_2}}{n_{\text{H}_2} + n_{\text{H}_2\text{O}}} \quad (9)$$

Significant carbon deposition also took place during the fuel stage and this deposited carbon was released in the steam and air stages. The fraction of carbon deposition is therefore quantified as follows based on the steam and air stages outlet and the total methane entering the fuel stage:

$$C_{\text{dep}} = \frac{n_{\text{CO}} + n_{\text{CO}_2}}{n_{\text{fuel, in}}} \quad (10)$$

The H_2 purity produced during the steam stage is determined by quantifying the amount of other gas present during the steam stage. It is therefore important that the steam stage is long enough to minimize the extent of the mixing of different gases. Hydrogen purity will be

reduced as a result of carbon deposition, possibly requiring further purification in a downstream processing step.

$$\sigma_{H_2} = \frac{n_{H_2}}{n_{H_2} + n_{CO} + n_{CO_2}} \Big|_{\text{steam}} \quad (11)$$

The CO_2 purity produced during the fuel stage is determined by quantifying the percentage of depleted air ($N_2 + O_2$) and unconverted fuel (CH_4) in the outlet gas stream during the fuel stage as

$$\sigma_{CO_2} = \frac{n_{CO_2}}{n_{CO_2} + n_{CO} + n_{N_2} + n_{O_2} + n_{\text{fuel}}} \Big|_{\text{fuel}} \quad (12)$$

Finally, the CO_2 capture efficiency is determined to quantify the percentage of CO_2 that escapes to the atmosphere during the air stage (100% minus the percentage of CO_2 that escapes to the atmosphere).

$$\eta_{CO_2} = 1 - \frac{n_{CO_2, \text{air}}}{n_{CO_2, \text{fuel}} + n_{CO_2, \text{air}} + n_{CO_2, \text{steam}}} \quad (13)$$

2.3. Oxygen carrier synthesis

As mentioned earlier, the water-splitting uses the different states oxides of iron to complete the cycle. Two campaigns to demonstrate GSWs concepts were completed with different iron based oxygen carriers. The first demonstration was completed with oxygen carrier of 35 wt% Fe_2O_3 supported on gamma-alumina. This oxygen carrier has shown very stable performance under redox conditions for methane reforming in a previous study [44]. In the second campaign, an optimized Cu-doped $Mg(Fe_{0.9}Al_{0.1})_2O_4$ spinel with 74 wt% active content was developed and investigated specifically for this study to meet the requirement of high active content loading for maximizing the separation performance of the GSWs process.

2.3.1. Synthesis of 1st campaign oxygen carrier (35 wt% Fe_2O_3 on Al_2O_3)

An oxygen carrier with 35% active Fe_2O_3 on Al_2O_3 was developed through wet impregnation where spherical gamma-alumina particles

from Sasol (Puralox SCCa 150/200) were impregnated in a concentrated aqueous ammonium iron(I) citrate solution (~50 g/100 g water). The aim was to form nanostructured iron oxide inside the mesoporous alumina structure after calcination. Homogenous distribution of the active iron oxide throughout the porous particles was obtained followed by drying steps at 120 °C after each step up to a theoretical loading of ~10 wt% metal oxide. After the drying, the material was subjected to heat treatment for about 5 h at 500 °C with ramp rate of 1 °C/min in ambient air. This procedure was repeated until the theoretical weight loading of the Fe active content to Al_2O_3 was about 1:1. The produced particles were sieved with 100 µm cut-off size to remove fines prior to quality assurance testing. SEM/EDS analysis on particles after sieving indicated the homogenous distribution of the Fe throughout the porous alumina structure (Fig. 5). The measured loading of active elements was lower than targeted (Fe:Al ≈ 0.55:1 by weight) due to the loss of active material by sieving, in form of fines which were loosely deposited on the surface of the particles. The BET surface area of the produced $Fe-Al_2O_3$, impregnated particles was measured to 102.9 m²/g in comparison with the bare alumina support particles with a BET surface area of 206.0 m²/g.

2.3.2. Synthesis of 2nd campaign oxygen carrier (Cu-doped $Fe/MgAl_2O_4$ spinel)

Iron oxide, magnesium carbonate, aluminum oxide, and copper oxide were weighed and dispersed in deionized water with a suitable dispersing agent to create a Cu-doped $Mg(Fe_{0.9}Al_{0.1})_2O_4$ spinel with 74 wt% active content. Wet ball milling using a horizontal attrition mill (Netzsch, Germany) was employed to homogenize the dispersion and create a stable suspension suitable for spray drying. The resulting slurry was spray-dried using a pressurized fountain-nozzle atomizing the suspension in the chamber of the spray dryer. The chamber was filled with hot air from the top resulting in a counter-current regime enabling rapid water evaporation forming spherical particles due to surface tension effects. To obtain oxygen carrier particles with sufficient mechanical strength and the desired crystalline phases, the resulting powder was then calcined at 1200 °C during 4 h to yield spheres with an average particle size of 150 µm and tap density of about 1.8 g/cm³.

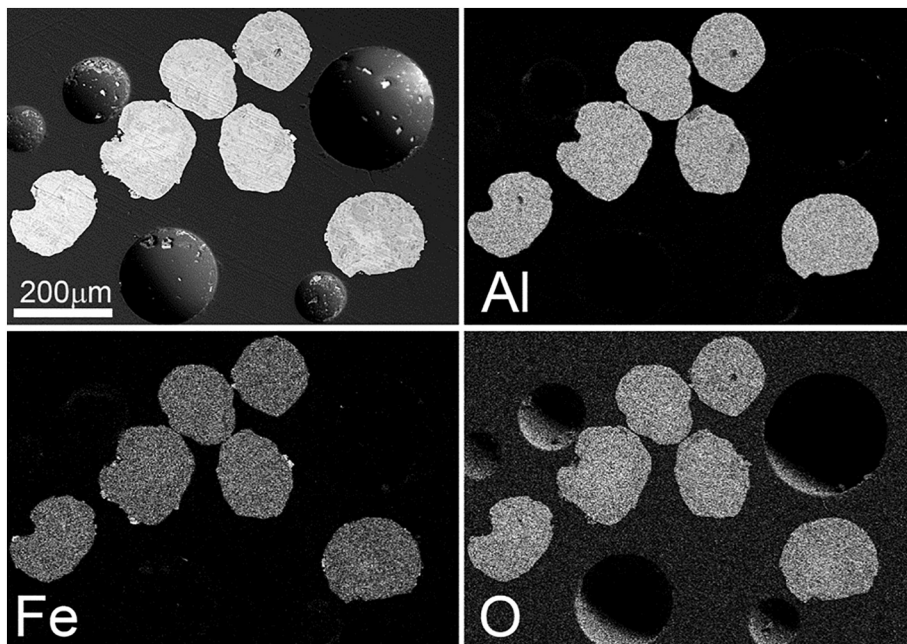


Fig. 5. SEM/EDS Image of the impregnated alumina particles with a map showing the distribution of Al, Fe and O content[44].

3. Results and discussion

GSWS experiments were completed with both oxygen carriers (35 wt% Fe_2O_3 on Al_2O_3 tested in a previous study on reforming but not water-splitting [44] and Cu-doped $\text{Fe/MgAl}_2\text{O}_4$ spinel with 74 wt% active content developed specifically for this study (section 3.2.2). Screening and characterization of the oxygen carrier were completed and redox experiments were carried out in the 5 cm ID fluidized bed reactor (Fig. 4) and TGA as explained in section 2.1. All experiments were conducted at atmospheric pressure.

3.1. 1st GSWS demonstration with $\text{Fe/Al}_2\text{O}_3$ OC of 35% wt Fe_2O_3

The first GSWS demonstration was done with the 5 cm ID fluidized bed reactor (Fig. 4) using 35% active Fe_2O_3 on Al_2O_3 as described in section 2.3.1. About 300 g of the oxygen carrier was initially placed in the reactor. Three-stage GSWS cycles (fuel, steam and air stages) were completed with CO and CH_4 as fuel at atmospheric pressure and temperatures between 700 and 900 °C. Fig. 6 shows a typical gas composition at the reactor outlet with repeatable behavior over several cycles with temperature profile as shown in SI Fig. S1. As presented in a previous study with the same oxygen carrier [44], the fuel stage occurs over two distinct sub-stages. Complete CO conversion was observed at the first sub-stage. This is in line with thermodynamics because CO is fully converted to CO_2 at equilibrium when Fe_2O_3 is present in the first sub-stage. However, CO conversion decreases to ~33% in the second sub-stage as the oxygen carrier is reduced beyond Fe_3O_4 . Despite the low conversion achieved in the second sub-stage of the fuel stage, a high degree of oxygen carrier utilization (from Fe_2O_3 to FeO) of about 80% was achieved. The large fuel slippage in the second sub-stage of the fuel stage could be treated properly by recycling or integrating to other downstream processes such as Gas Switching combustion, GSC [40,60] or reforming, GSR [50,61], to maximize fuel utilization and process efficiency. Indeed, a previous thermodynamic assessment of the GSC concept integrated with an IGCC power plant [62] assumed a maximum achievable reactor temperature of 1200 °C, even though state of the art gas turbines can operate well above 1400 °C. Despite this negative aspect, the GSC concept easily outperformed conventional pre-combustion CO_2 capture, achieving 4%-points higher efficiency [62]. This efficiency advantage can be extended by several additional %-points through an additional combustor after the GSC reactors [63]. H_2 from the GSWS reactors can be used to fuel this combustor and raise the stream temperature to the maximum achievable turbine inlet temperature. This process configuration can, therefore, achieve very high

electric efficiencies, while accommodating a large amount of fuel slip in the GSWS fuel stage.

As for the subsequent steam stage, steam conversion of about 30% was achieved, which is higher than equilibrium predictions with FeO [3,20,64], indicating some degree of oxygen carrier reduction to metallic Fe. However, steam conversion decreased later in the stage as the active sites available for partial oxidation with steam diminished. It was also observed from Fig. 6, that no other gas was produced during the steam stage that would contaminate the produced H_2 before switching to another stage, thus making the process promising with the potential of producing high purity H_2 (over 95%).

At the air stage, some traces of CO_2 were produced indicating some carbon deposition in the previous reduction stage. As a result, CO_2 capture efficiency was affected through the release of CO_2 with a stream of depleted air (N_2) at the air stage since CO_2 is captured only during the fuel stage. Fortunately, the deposited carbon could not be gasified during the steam stage thus not affecting H_2 purity. Fig. 6 also shows that O_2 composition approached 21% at the end of the air stage implying that the oxygen carrier was completely oxidized before the start of the next redox cycle. One of the advantages of the GST reactor design like the conventional chemical looping reactor is the capability of preventing deactivation of the oxygen carrier through coking as the deposited carbon are gasified and combusted completely at the air stage before the start of the next cycle.

The sensitivity of steam conversion and oxygen carrier utilization to the reduction time is shown in Fig. 7 a. It could be seen that the oxygen carrier utilization increased only by ~17% when the reduction time was doubled and by ~32% with tripling of the reduction time. The relatively slow increase in oxygen carrier utilization with reduction time originates from the large fuel slippage that occurs when the reduction time is higher than 2 min. Despite this small increase in the oxygen carrier utilization, it has substantially improved the extent of steam conversion to hydrogen. The average steam conversion across the whole steam stage has increased by ~2.9× when the reduction time was doubled implying a ~5.8× increase the quantity produced in the 3 min reduction time. As for the 9 min reduction time, the average steam conversion remained relatively unchanged in comparison to the 6 min, but the H_2 yield has increased by 50% in comparison to the 6 min (the oxygen carrier utilization has only increased by ~11% opening about 0.145mols additional FeO sites for water-splitting reaction) and is ~8.79 times the 3 min reduction time. This large increase in H_2 yield despite the limited increase in the oxygen carrier utilization could be explained by the creation of Fe sites on the reduced oxygen carrier that have much higher steam equilibrium conversion to H_2 than FeO [65,66]. This can clearly be seen in Fig. 8 showing that the transient steam conversion to H_2 peaks in the beginning of the steam stage to values beyond equilibrium predictions of FeO demonstrating existence of Fe sites (with higher extents for the case of 9 min reduction time), but it goes down across the stage as the Fe sites are being consumed. This positive improvement in steam conversion to H_2 would justify accommodating the large fuel slippage occurring in the reduction stage if fuel recycling or GSWS process integration measures are implemented to maximize fuel conversion and energy efficiency.

The increased operating temperature has shown a positive effect on fuel conversion in the reduction stage, leading to increased oxygen carrier utilization (Fig. 7 b) in line with thermodynamics and likely due to improved kinetics [67]. This enhanced the degree of reduction of the oxygen carrier improving steam conversion to H_2 . This phenomenon counteracts the negative effect of increased temperature on equilibrium of water splitting reaction (Eq. 3 and Eq. 4) over iron and its oxide.

Further testing of the GSWS concept using CH_4 as fuel shows repeatable cyclic performance (Fig. 9). The major difference observed with CH_4 is that two distinct phenomena occur during the fuel stage. First is the reduction reaction from Fe_2O_3 to FeO associated with CO_2 production. As the lattice oxygen continues to deplete, a point is reached where the reaction switches completely to partial oxidation of methane

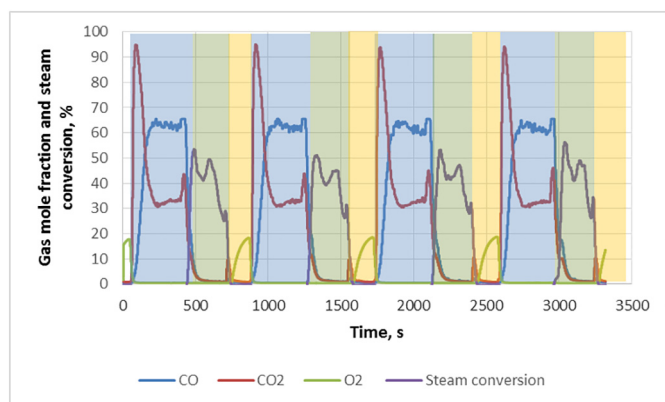


Fig. 6. The transient gas composition of 4 cycles of GSWS using CO as fuel at 900 °C and 1 bar. Fuel stage in blue; Steam stage in green; Air stage in yellow. Flowrate: 5 NL/min CO for 6 min (80% degree of OC reduction), 1.9 NL/min steam for 5 min (CO: steam molar ratio feeds = 2.5), 10NL/min Air for 3 min. (For interpretation of the references to colour in this figure legend, the reader is referred to the web version of this article.)

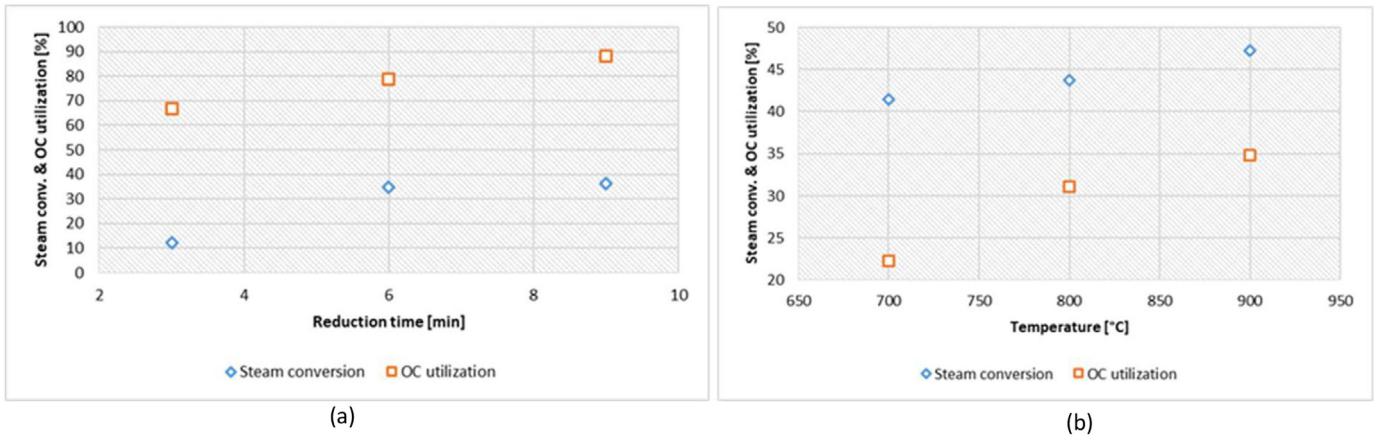


Fig. 7. a) The sensitivity of average steam conversion to oxygen carrier utilization of GSWS process using CO as fuel. Fuel stage (5 NL/min pure CO); steam stage (1.9 NL/min); Air stage (10 NL/min). All the stages were completed at 900 °C and 1 bar. b) The sensitivity of average steam conversion to operating temperature of GSWS process at 1 bar. Fuel stage (5 NL/min pure CO for 3 min), steam stage (1.9 NL/min for 5 min); Air stage (10 NL/min for 3 min).

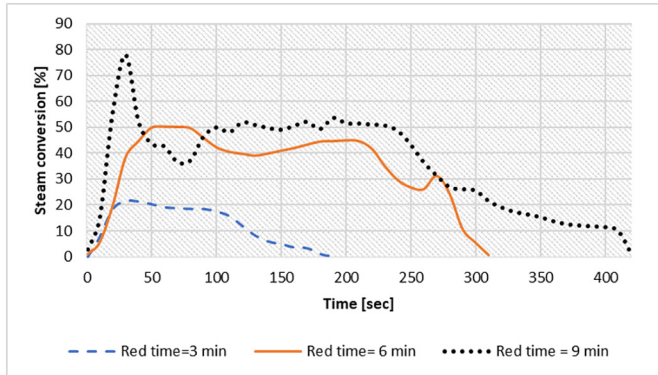


Fig. 8. The transient steam conversion to H₂ with reduction time. Fuel stage (5 NL/min pure CO); steam stage (1.9 NL/min); Air stage (10 NL/min). All the stages were completed at 900 °C and 1 bar.

associated with syngas production of H₂:CO ratio of approximately 2:1. About 60% fuel conversion was achieved in the first phase (reduction phase) of the fuel stage while CH₄ conversion further drops to about

40% in the 2nd phase (POX) of the fuel stage in line with thermodynamic analysis of Dohyung Kang et al. [68]. At the start of the steam stage, CO was produced through the gasification of the deposited carbon in the previous fuel stage. This phenomenon increases the partial pressure of CO shifting the equilibrium of Boudouard reaction to the right to convert the produced CO to CO₂ and redepositing carbon. The CO and CO₂ concentration in the steam thus affect H₂ purity negatively. This could be due to the steam gasification of the deposited carbon at the steam stage.

3.2. 2nd GSWS demonstration with Cu-doped Fe/MgAl₂O₄ spinel OC

3.2.1. Oxygen carrier chemistry and screening

From Fig. 3 it is clear that an oxygen carrier with 35 wt% of redox-active Fe₂O₃ is not sufficient to obtain hydrogen of high purity at elevated operating pressures. Initially, it was planned to produce oxygen carriers via spray-drying using promising material formulations (based on Fe₂O₃) that have been reported in the literature in the context of chemical looping water-splitting [9,32,69]. The majority of these materials showed good cyclic stability only with low Fe₂O₃ contents (<30 wt%) and/or under mild reaction conditions (<900 °C) with incomplete conversion of the oxygen carrier. Further, only a few studies dealt with

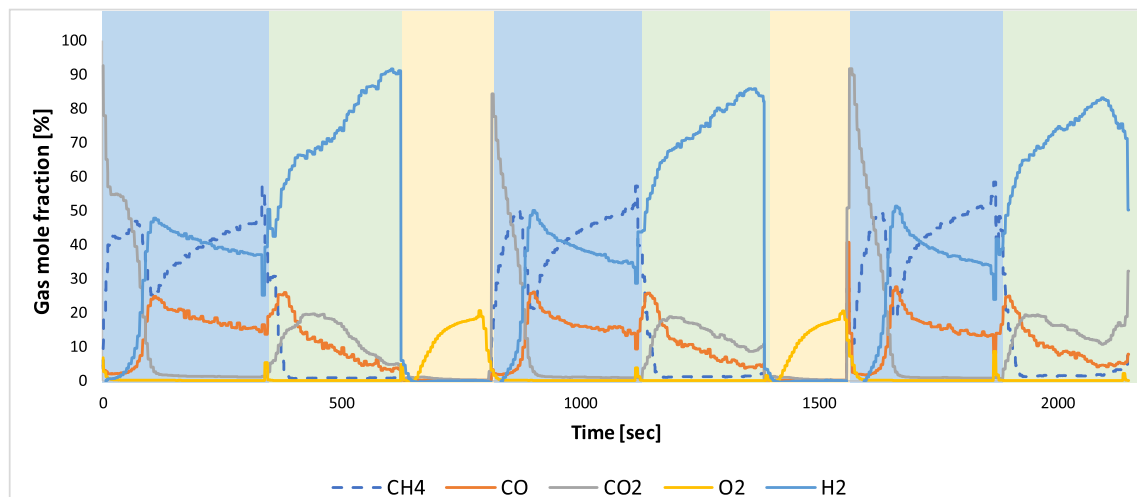


Fig. 9. The transient gas composition of 4 GSWS cycles with CH₄ as fuel. Fuel stage in blue, steam stage in green, air stage in yellow. Flowrate: 1.7 NL/min CH₄ for 6 min; 1.9 NL/min steam for 5 min (H₂O:CH₄ molar ratio = 3:1), 10NL/min air for 3 min. (For interpretation of the references to colour in this figure legend, the reader is referred to the web version of this article.)

using CH_4 during reduction, which has a much lower reactivity with Fe_2O_3 than CO or H_2 , and hardly any work investigated the suitability of the oxygen carriers for fluidized bed reactors, where also mechanical properties are important. Most importantly, sintering and agglomeration of oxygen carrier particles has widely been neglected but is arguably the most important aspect when using oxygen carrier particles in a fluidized bed system at a large scale. Agglomeration of particles in the reactor would terminate operation immediately. Almost none of the previous works on oxygen carrier development addressed challenges associated with scale-up and actual large-scale operation. Specifically, the oxygen carrier particles had to possess high oxygen storage capacity ($> 0.2 \text{ g O}_2$ per g OC, corresponding to $\sim 70 \text{ wt\% Fe}_2\text{O}_3$ in the oxygen carrier), high reactivity with CH_4 , high resistance towards sintering at high temperature (up to 1000°C), high resistance towards coke deposition that would contaminate the H_2 generated in the subsequent steam oxidation step, and reasonable mechanical strength ($\sim 50 \text{ MPa}$). The material formulation had to be suitable for a production process via spray-drying, followed by calcination at high temperature (1200 – 1300°C) to ensure sufficient mechanical strength. The resulting oxygen carrier particles produced through spray-drying are naturally of very low surface area ($< 1 \text{ m}^2/\text{g}$), which requires good solid-state properties to achieve high reactivity [70].

The cyclic performance of newly developed oxygen carriers (their synthesis is described in the experimental section 2.3.2) was assessed using thermogravimetric analysis (TGA) at 850°C and they were characterized by electron microscopy and X-ray diffraction (XRD) before and after the cycling experiments.

3.2.1.1. Material development and assessment of the cyclic redox performance in the TGA. The material development work focused initially on Fe_2O_3 supported on La-doped CeO_2 and variations thereof [56,71–73]. When cycled in the TGA at 850°C , none of them was found to be cyclically stable and the oxygen carriers deactivated quickly due to sintering (data not shown in this work). Promising results were reported by Imtiaz et al. [74], and so similar oxygen carriers were produced from nitrates, which contained $70 \text{ wt\% Fe}_2\text{O}_3$, $22 \text{ wt\% MgAl}_2\text{O}_4$ and 8 wt\% CuO . Cu-species have high mobility and they were found to migrate to the surface and cover Fe-sites during reduction, thus reducing their catalytic effect for CH_4 decomposition ($\text{CH}_4 \rightarrow \text{C} + 2\text{H}_2$) substantially [74]. The oxygen carriers produced in this work were calcined at much higher temperature than in the original work by Imtiaz et al. due the requirement for obtaining stable spheres after spray-drying in a scaled production process; the corresponding X-ray diffractograms are compared in Fig. 10 a – c.

It is clear that at the lower calcination temperatures, both Fe_2O_3 (PDF 01–080–5406) and a cubic (Mg,Al,Fe) spinel phase existed within the oxygen carrier (Fig. 10 a & b). A crystalline CuO phase was not observed, suggesting the dissolution of CuO in the spinel phase. With increasing calcination temperature, there was a gradual decrease in the amount of Fe_2O_3 and after calcination at 1300°C (Fig. 10 c), almost all Fe_2O_3 existed in a mixed (Mg,Al,Fe) spinel phase (identified as $\text{Mg}(\text{Fe}_{0.5}\text{Al}_{0.5})_2\text{O}_4$, PDF 01–080–3010), which most likely included also the Cu, since no reflections from isolated CuO were detected. If CuO is incorporated in the spinel structure, its mobility is lowered and all elements within the spinel structure are effectively anchored [75]. It was recently

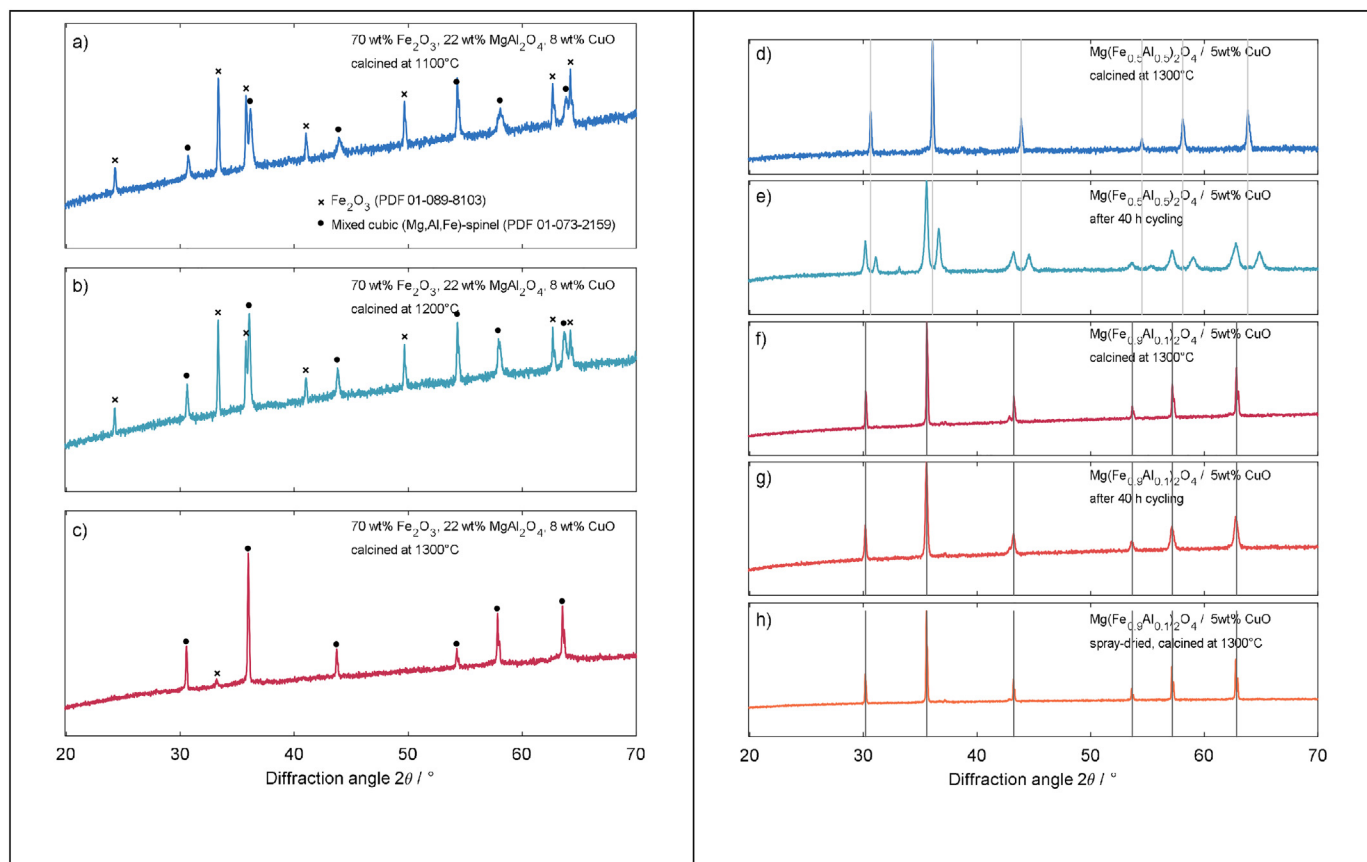


Fig. 10. The results from X-ray diffraction. a) – c) Effect of calcination temperature on the crystalline phases formed for an oxygen carrier with $70 \text{ wt\% Fe}_2\text{O}_3$, $22 \text{ wt\% MgAl}_2\text{O}_4$ and 8 wt\% CuO . d) As-prepared oxygen carrier $\text{Mg}(\text{Fe}_{0.5}\text{Al}_{0.5})_2\text{O}_4$ with 5 wt\% CuO calcined at 1300°C . e) Oxygen carrier $\text{Mg}(\text{Fe}_{0.5}\text{Al}_{0.5})_2\text{O}_4$ with 5 wt\% CuO calcined at 1300°C after 40 h of redox cycling in the TGA at 850°C . f) As-prepared oxygen carrier $\text{Mg}(\text{Fe}_{0.5}\text{Al}_{0.5})_2\text{O}_4$ with 5 wt\% CuO calcined at 1300°C . g) Oxygen carrier $\text{Mg}(\text{Fe}_{0.5}\text{Al}_{0.5})_2\text{O}_4$ with 5 wt\% CuO calcined at 1300°C after 40 h of redox cycling in the TGA at 850°C . h) Spray-dried, as-prepared oxygen carrier $\text{Mg}(\text{Fe}_{0.5}\text{Al}_{0.5})_2\text{O}_4$ with 5 wt\% CuO calcined at 1300°C . The vertical light grey lines in d) and e) indicate the peak positions of the reference pattern for $\text{Mg}(\text{Fe}_{0.5}\text{Al}_{0.5})_2\text{O}_4$, PDF 01–080–3010. The vertical dark grey lines in f) – h) indicate the peak positions of the reference pattern for $\text{Mg}(\text{Fe}_{0.5}\text{Al}_{0.5})_2\text{O}_4$, PDF 01–071–1233.

shown that Cu can be exsolved from the spinel under reducing conditions, thereby improving the material's reactivity [76]; this is discussed below together with results from the in-situ XRD measurements.

Owing to the formation of the mixed spinel phase upon calcination at high temperature, a stoichiometric compound was synthesized and used as an oxygen carrier, $\text{Mg}(\text{Fe}_{0.5}\text{Al}_{0.5})_2\text{O}_4$ doped with 5 wt% CuO (calcined at 1300 °C). From the XRD pattern presented in Fig. 10 d the oxygen carrier was nearly phase-pure and the corresponding EDX maps shown in Fig. 11 confirm a uniform distribution of elements within the material. Measurements via ICP-OES gave a ratio of Mg:Fe:Al:Cu of 0.310:0.585:0.061:0.044, which was in good agreement with the theoretical ratio (Mg:Fe:Al:Cu = 0.320:0.575:0.064:0.041).

The oxygen carrier was cycled (reduction in ~7 vol% CH_4 and oxidation in ~83 vol% air) in the TGA at 850 °C, with the results of the first eight cycles shown in Fig. 12 a & b. Initially, there was hardly any reduction (Fig. 12 a), but the oxygen carrier gradually activated, as can be seen from the increasing weight loss during reduction. The subsequent weight increase measured during reduction was due to the decomposition of CH_4 , resulting in coke deposits on the surface of the oxygen carrier. The weight loss curve thus reflects two different mechanisms: The loss of lattice oxygen due to the conversion of CH_4 , and a weight increase due to coke depositing on the sample surface. After 30 cycles, the measured oxygen storage capacity prior coking was ~10.9 wt%, which corresponds to 76% of the theoretical oxygen storage capacity assuming the equivalent amounts of Fe_2O_3 and CuO were the only redox-active species. It was thus expected that coking would not become a major problem in fluidized bed experiments by limiting the time of

the reduction since the oxygen carrier is reduced uniformly inside the reactor.

Fig. 10 d & e compare the diffractograms acquired before and after the cycling experiment respectively. The peaks corresponding to the (Cu-doped) $\text{Mg}(\text{Fe}_{0.5}\text{Al}_{0.5})_2\text{O}_4$ spinel split into pairs of peaks, indicating the separation of the $\text{Mg}(\text{Fe}_{0.5}\text{Al}_{0.5})_2\text{O}_4$ spinel into an Fe-rich and an Fe-depleted spinel phase. The Fe-rich spinel phase was identified as $\text{Mg}(\text{Fe}_{0.9}\text{Al}_{0.1})_2\text{O}_4$ spinel (PDF 01-071-1233), containing theoretically 74 wt% of redox-active Fe_2O_3 . Since this phase appeared to be the thermodynamically stable phase under the reaction conditions employed, a phase pure $\text{Mg}(\text{Fe}_{0.9}\text{Al}_{0.1})_2\text{O}_4$ oxygen carrier doped with 5 wt% CuO was synthesized and investigated in the TGA under identical reaction conditions. The results are plotted in Fig. 12 c & d and show that the material was active from the first cycle and no activation period was required. The diffractogram of the oxygen carrier after the cycling experiment (after 60 cycles after the air oxidation step, corresponding to ~40 h of cycling operation) was identical with that of the as-synthesized oxygen carrier, demonstrating that no irreversible phase changes occurred during redox cycling (Fig. 10 f & g). The extent of coking was much lower than that seen for the Cu-doped $\text{Mg}(\text{Fe}_{0.5}\text{Al}_{0.5})_2\text{O}_4$ and the oxygen storage capacity was 18.8 wt%, utilizing ~85% of the total redox-active lattice oxygen prior coking. The material collected from the TGA after the 60 cycle experiment appeared fused together (note that fine powder was used as the starting material) and could not easily be separated by slight agitation, confirming that surface area played only a minor role for the material's reactivity. In the TGA experiments, fine powder of oxygen carrier remained stagnant in the crucible during

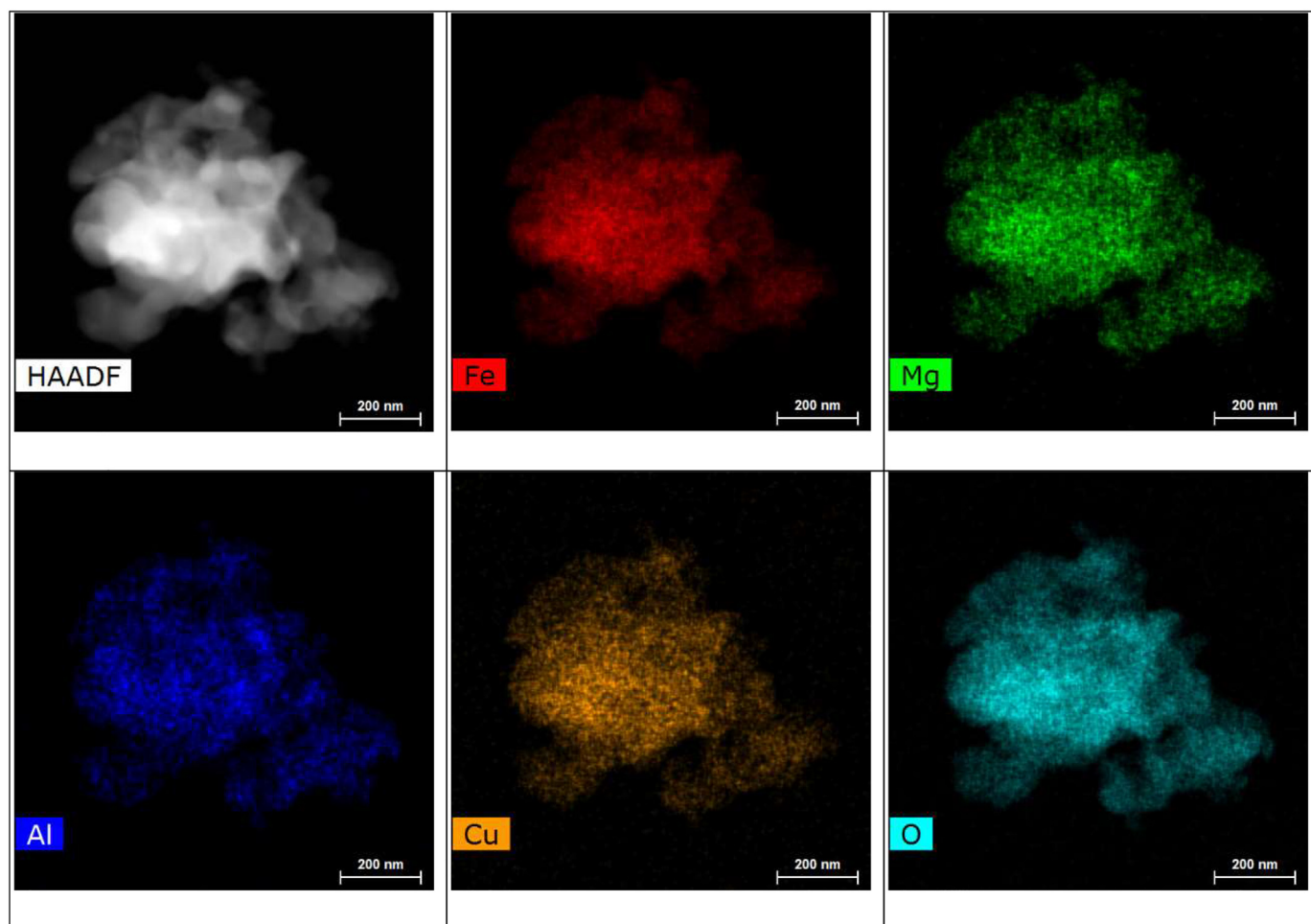


Fig. 11. TEM images of the as-prepared oxygen carrier $\text{Mg}(\text{Fe}_{0.5}\text{Al}_{0.5})_2\text{O}_4$ with 5 wt% CuO calcined at 1300 °C, and the corresponding elemental maps.

redox cycling, which clearly facilitated sinter processes. In fluidized bed operation, discussed below in [section 3.2.2](#) the oxygen carrier particles were much larger (100–180 μm) and under vigorous movement with fast heat transfer; it was thus expected that sinter processes causing particle agglomeration would not be significant or could at least be controlled by varying the flow rate of gas and the extent of reduction.

3.2.1.2. Material characterization. Most oxygen carriers deactivate owing to either irreversible phase changes occurring during redox cycling or sintering decreasing the surface area and accessible pore-volume, or both. From the TGA experiments it appeared that the reactivity of the Cu-doped $\text{Mg}(\text{Fe}_{0.9}\text{Al}_{0.1})_2\text{O}_4$ oxygen carrier particles did not depend on surface area (N_2 sorption measurements of fresh and cycled material gave BET surface areas $<1 \text{ m}^2/\text{g}$). Since no irreversible phase changes occurred during redox cycling ([Fig. 10f&g](#)), the oxygen carrier was inherently stable.

The experiments described above have, so far, neglected the re-oxidation with steam to produce H_2 . Using high steam concentrations in TGAs is usually difficult, and so CO_2 was used as an oxidant instead. At 850°C , CO_2 and H_2O possess roughly the same oxidation potential [76]. [Fig. 13 a & b](#) show the results from a TGA experiment (first five redox cycles), where the Cu-doped $\text{Mg}(\text{Fe}_{0.9}\text{Al}_{0.1})_2\text{O}_4$ oxygen carrier was reduced in CH_4 and re-oxidized using first CO_2 and then air. Oxidation with CO_2 restored 89% of the total redox-active lattice oxygen of the material within the given time. Nonetheless, a significant amount of heat was produced when replenishing the remaining lattice oxygen with air, with the oxidation in CO_2 being nearly heat neutral ([Fig. 13 b](#)). No adverse effects on the cyclic redox stability have been observed when the oxygen carrier was not re-oxidized in air, although it has been reported for mixed Fe-based oxygen carriers that an air oxidation

step may be required [76] to prevent the material's deactivation due to gradual phase segregation. Material collected from the TGA appeared less sintered compared to that which had been re-oxidized using air only, implying that the re-oxidation with CO_2 (or steam in the actual hydrogen generation step) aided in restoring transient phases of lower sinter temperatures.

Temperature-programmed reduction (TPR) in the presence of 7 vol% CH_4/N_2 using the TGA showed that the Cu-doped $\text{Mg}(\text{Fe}_{0.9}\text{Al}_{0.1})_2\text{O}_4$ oxygen carrier reduced in two principal steps ([SI Fig. S2 c](#)). The results were confirmed by in-situ XRD ([Fig. 13 c](#)), which was performed under similar reaction conditions as the cycling experiment (i.e. reduction with CH_4 , oxidation with CO_2 followed by air at 850°C). [Fig. 13 c](#) shows that upon exposure to CH_4 , the oxygen carrier reduced to metallic iron via a different mixed (Mg,Al,Fe) phase. Interestingly, separate reflections from Cu-species were not seen until also metallic iron formed. Separate crystalline Al-containing phases such as Al_2O_3 were not detected during reduction. Upon re-oxidation with CO_2 (scans 32–46 in [Fig. 13 c](#) metallic Cu (peak near 50°) was re-incorporated in the mixed spinel environment, which is different from what has been observed for Fe-based brownmillerite structures, where Cu could only be re-incorporated upon exposure to air (i.e. at higher partial pressures of oxygen) [76]. Before the atmosphere in the reaction chamber was changed from CO_2 to air, there was, somewhat unexpected, a gradual transition towards the initial spinel phase, which suggests that a near-complete recovery of lattice oxygen with CO_2 was possible. To confirm this, an isothermal cycling experiment was performed at 850°C , in which after the fourth reduction the material was re-oxidized for 4 h in 20 vol% CO_2 only ([SI Fig. S2 c](#)). Indeed, there was an increase in sample mass throughout the oxidation period, although at a very low rate that would prevent the complete re-oxidation with a reasonable time. However, this

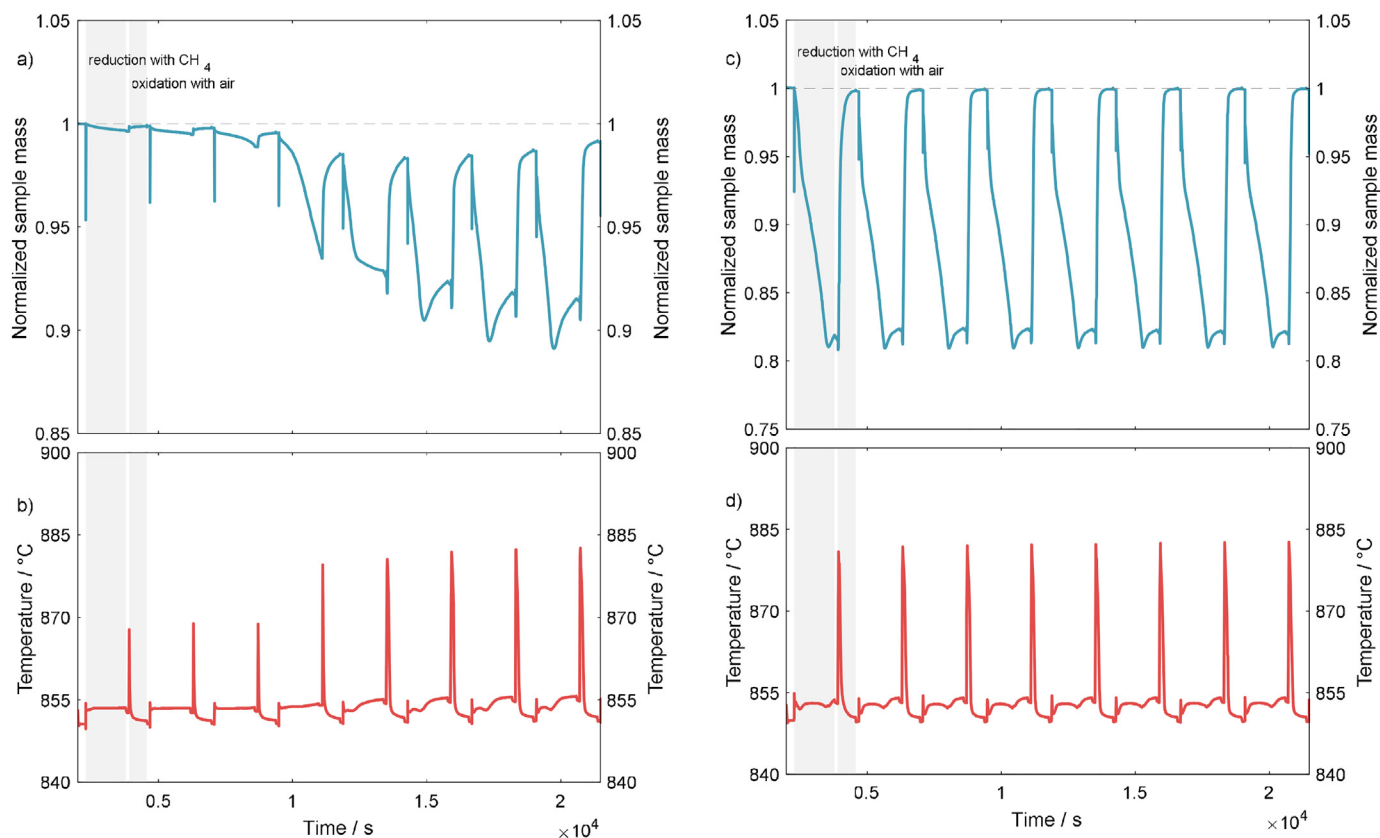


Fig. 12. The results from the redox cycling experiments using the TGA at 850°C . Reduction was performed with CH_4 and oxidation was performed with air. a) and b) show the normalized sample mass and sample temperature, respectively, measured during the initial eight (of 60) cycles for the oxygen carrier $\text{Mg}(\text{Fe}_{0.9}\text{Al}_{0.5})_2\text{O}_4$ with 5 wt% CuO. c) and d) show the normalized sample mass and sample temperature, respectively, measured during the initial eight (of 60) cycles for the oxygen carrier $\text{Mg}(\text{Fe}_{0.9}\text{Al}_{0.1})_2\text{O}_4$ with 5 wt% CuO.

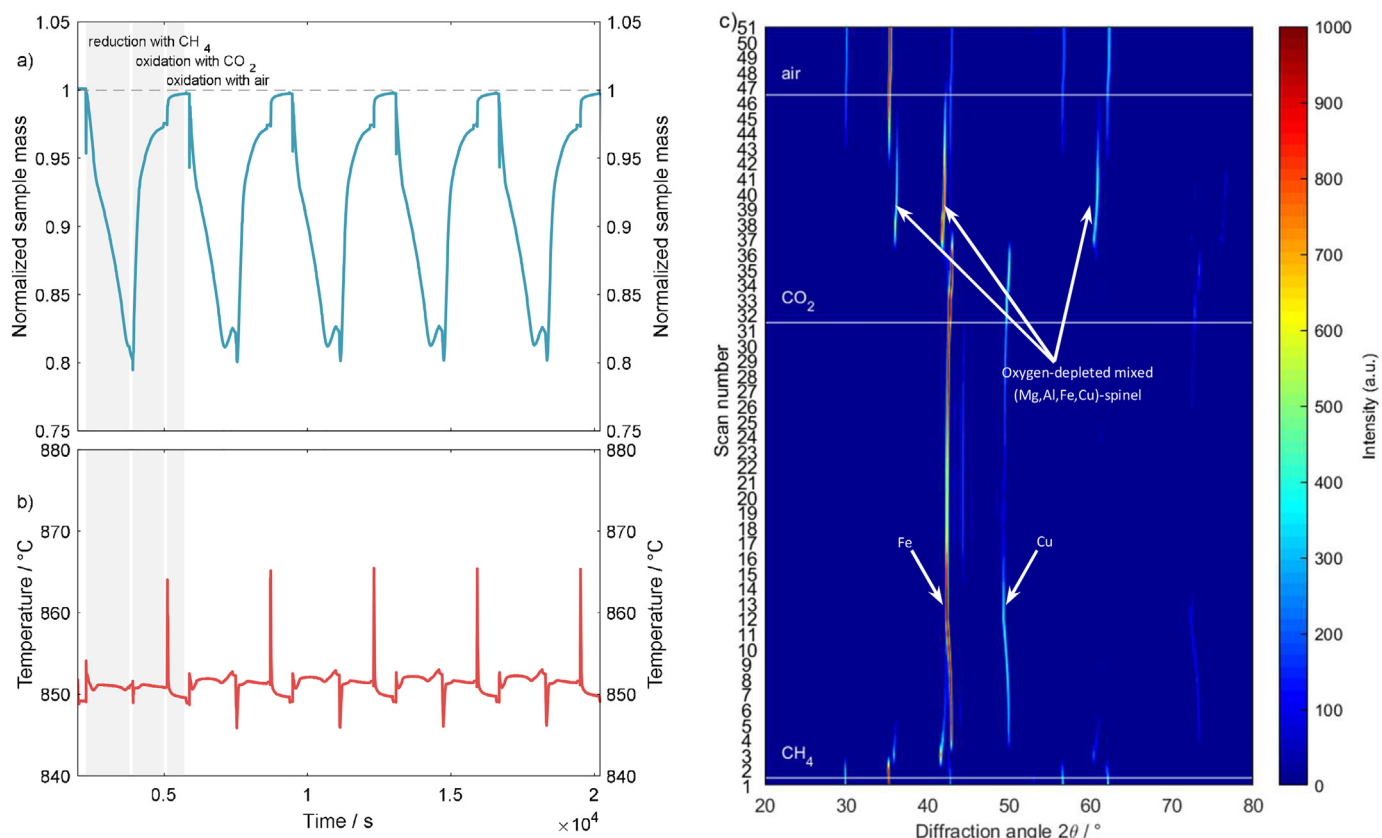


Fig. 13. The results from the redox cycling experiments using the TGA and In-situ XRD at 850°C . a) and b) show the normalized sample mass and sample temperature, respectively, measured during the initial five cycles for the oxygen carrier $\text{Mg}(\text{Fe}_{0.9}\text{Al}_{0.1})_2\text{O}_4$ with 5 wt% CuO. c) shows a 2D intensity map measured during an in-situ XRD experiment at 850°C in which the oxygen carrier $\text{Mg}(\text{Fe}_{0.9}\text{Al}_{0.1})_2\text{O}_4$ with 5 wt% CuO was reduced in CH_4 (scans 2–31) and oxidized in CO_2 (scans 32–46) and oxidized in air (scans 47–51).

result also implies that the complete combustion of CH_4 to generate CO_2 and H_2O only during the reduction of the fully-oxidized oxygen carrier (as is the case for the transition $\text{Fe}_2\text{O}_3 \rightarrow \text{Fe}_3\text{O}_4$) is probably not possible thermodynamically. At the beginning and the end of the in-situ XRD experiment (scan 1 and 51), the same crystalline spinel phase (PDF 01–071–1233) was observed, confirming the fully reversible phase changes within the oxygen carrier.

In the actual gas switching reactor, a fluidized bed, spray-dried particles were used (their synthesis is described in the experimental section 3.2.2. Most of the freshly calcined particles were of spherical shape, but

some particles had the shape of a torus with a large void in the center, as can be seen in Fig. 14 a. In addition, smaller satellite particles stuck to larger ones, thus forming agglomerates of particles. The compression strength of the as-synthesized spray-dried Cu-doped $\text{Mg}(\text{Fe}_{0.9}\text{Al}_{0.1})_2\text{O}_4$ oxygen carrier particles was 4.25 ± 1.29 N, which is equivalent to ~ 142 MPa when normalizing force by the average geometrical diameter of the particles. The relatively large standard deviation of the measured crushing strength was probably due to the inhomogeneity of some of the particles, as seen in Fig. 14 a. After 60 redox cycles in the TGA, the crushing strength reduced to 3.44 ± 1.46 N (equivalent to ~ 115

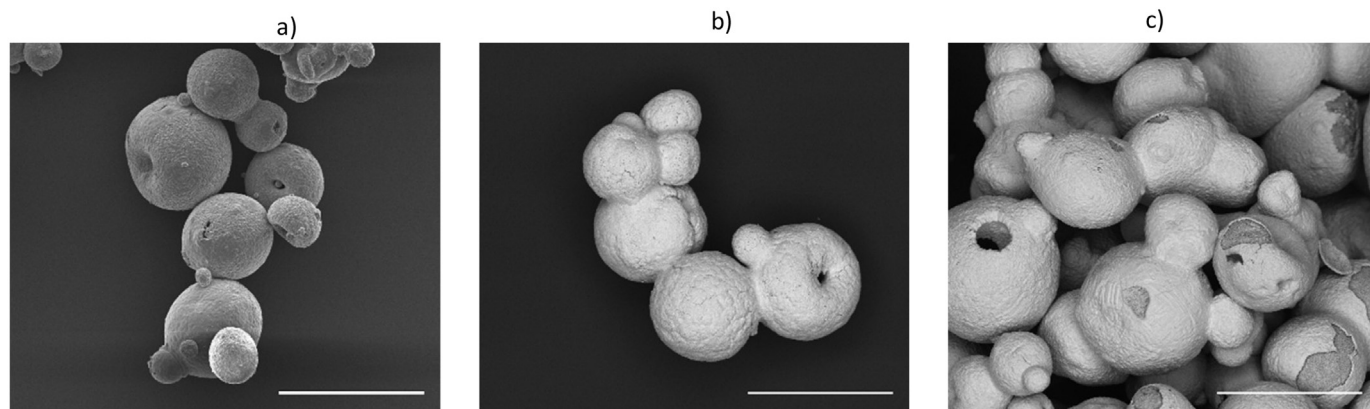


Fig. 14. SEM images of the spray-dried oxygen carrier $\text{Mg}(\text{Fe}_{0.9}\text{Al}_{0.1})_2\text{O}_4$ with 5 wt% CuO. a) As-prepared oxygen carrier particles, b) oxygen carrier particles after redox cycling in the fluidized bed, and c) oxygen carrier particles after redox cycling in the fluidized bed when the bed partially defluidized and the oxygen carrier particles fused together. The length of the white bar is 200 μm .

MPa), which is comparable to what has been reported as state-of-the-art in the context of oxygen carriers for chemical looping [77].

3.2.2. Fluidized bed experiment with optimized Cu-doped $\text{Mg}(\text{Fe}_{0.9}\text{Al}_{0.1})_2\text{O}_4$ spinel OC

The oxygen carrier material was investigated in the 5 cm ID reactor (Fig. 4) under atmospheric condition. The mass of the oxygen carrier originally placed in the reactor was 460 g making about 3 mol of lattice oxygen. It is important to note the reduction behavior and the thermodynamic properties of the Cu-doped $\text{Mg}(\text{Fe}_{0.9}\text{Al}_{0.1})_2\text{O}_4$ are fundamentally different from the Fe_2O_3 -system, for which three-phase transitions occur upon reduction (Fe_2O_3 - Fe_3O_4 , Fe_3O_4 -Fe, FeO-Fe). Cu-doped $\text{Mg}(\text{Fe}_{0.9}\text{Al}_{0.1})_2\text{O}_4$ reduces in two steps, where the first step (transition between two different spinel environments, Fig. 10 c) would require the consumption $\sim 1/3$ of the total redox-active lattice oxygen (Fig. 12 a), equivalent to $\text{Fe}_2\text{O}_3 \rightarrow \text{FeO}$ transition. In the second transition the redox-active Fe-species transform from the spinel environment to metallic Fe at a relatively low equilibrium constant (equivalent to $\text{FeO} \rightarrow \text{Fe}$ transition), which implies that upon reduction no pure CO_2 can be generated, but upon oxidation with steam even higher yields of H_2 can be obtained than for the transition $\text{Fe} \rightarrow \text{FeO}$. In fact, in preliminary studies the measured equilibrium constant $K_{eq} = p\text{CO}_2/p\text{CO}$ (CO_2 was used as a surrogate for H_2O) at 800°C was 0.33 compared to $K_{eq} = 0.54$ for the transition $\text{Fe} \rightarrow \text{FeO}$.

3.2.2.1. Reactor performance. From Fig. 15 the cyclic behavior of the oxygen carrier was repeatable over the three cycles. The degree of fuel conversion in the fuel stage was, unfortunately, low, with a large quantity of unconverted CH_4 , CO and H_2 exiting the reactor. It is possible that conversion will be improved in a larger reactor with a greater gas residence time, but the general degree of fuel utilization in these experiments was below expectations when comparing it with the results from the TGA experiments (Fig. 12 c). It is clear that such a large amount of fuel slip will require integration with another process capable of combusting this large quantity of slipped fuel as discussed earlier. From Fig. 15, about 13% steam conversion was achieved at 800°C , which was much lower than expected from K_{eq} (note that $K_{eq} = 0.33$ implies a steam conversion of 75% is feasible). It thus appeared that the oxygen carrier was not reduced sufficiently to exploit the low value of K_{eq} for this material. Carbon deposition from the fuel stage was also eminent and unlike the behavior with the oxygen carrier containing 35 wt% Fe_2O_3 , the

deposited carbon was gasified in the steam stage to produce syngas ($\text{CO} + \text{H}_2$), thus reducing the H_2 purity.

Even though such large degrees of fuel slip can be accommodated by more complex process integration, it remains desirable to greatly improve the fuel utilization in the GSWS fuel stage. High fuel conversion, therefore, remains an important priority for future oxygen carrier development studies. Apart from the low fuel utilization, the new oxygen carrier presented additional challenges in the reactor tests: agglomeration (Fig. 14 b & c) at higher degrees of reduction and carbon deposition in all cases. When the fuel time was increased beyond 4 min, the oxygen carrier started to agglomerate at the air stage after 10 cycles (SI Fig. S3). This was probably because of non-uniform reduction arising from dead zones in the reactor above the distributor plate, making some part of the oxygen carrier much more reduced than others. This phenomenon made the reactor inoperable. The produced agglomerate was brittle and could relatively easily be reduced to a fluidizable and reactive powder again. It is also desired to reduce the oxygen carrier uniformly in the bed to prevent coking as seen in the TGA experiments section 3.2.1 (Fig. 12 c).

However, it is very important for the GSWS process to be able to achieve a large degree of oxygen carrier utilization to maximize CO_2 separation efficiency. As outlined in the introduction, lower degrees of oxygen carrier utilization will magnify the effect of the mixing of different gases when switching between stages, resulting in lower CO_2 capture efficiency and purities of H_2 and CO_2 . As illustrated later in the achieved oxygen carrier utilization in the case with 4 min fuel time was only 34% (Fig. 16), implying that the onset of agglomeration at the oxidation stage is greatly restricting the degree of oxygen carrier utilization and thus also the CO_2 separation performance of the reactor. This is in agreement with the TPR results (SI Fig. S2) and in-situ XRD experiments (Fig. 13 c). The onset of both coking and agglomeration appears to be related to the formation of the metallic iron phase.

As outlined in section 3.2.1 agglomeration was observed in TGA experiments only when a fine powder was used. It is therefore difficult to ascertain why agglomeration of the spray-dried particles was experienced in the larger reactor, but one possibility could be the large reactor aspect ratio, which limited the axial mixing in the reactor. Lower quality of mixing will increase the likelihood of particle agglomerates forming. Agglomeration will be a self-strengthening phenomenon in this case, with initial agglomerates further reducing the quality of mixing in the bed, thus allowing additional agglomerates to form.

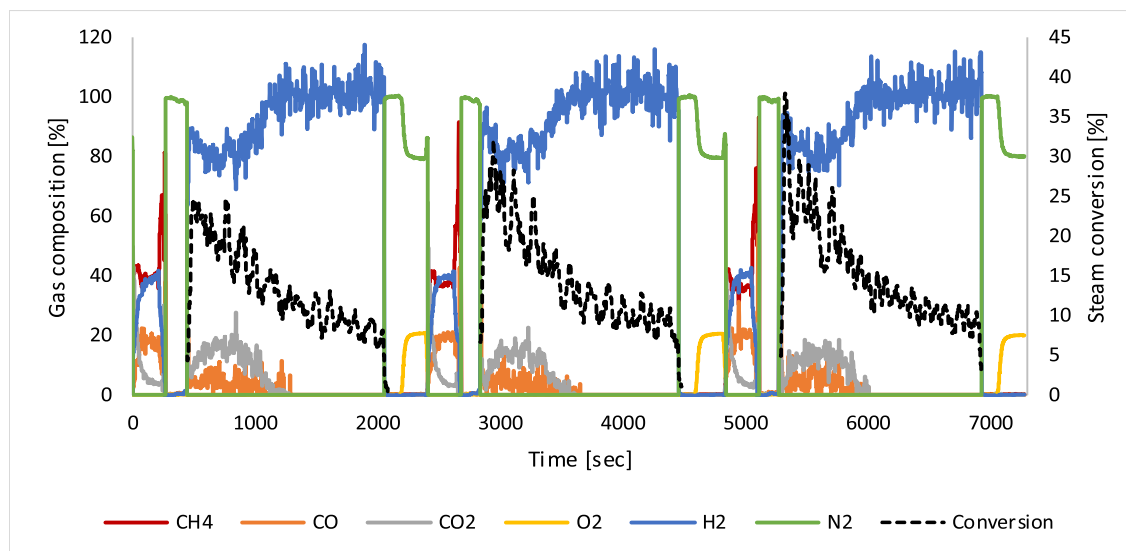


Fig. 15. Three cycles of reactor operation with a fuel time of 4 min at 800°C and 1 bar.

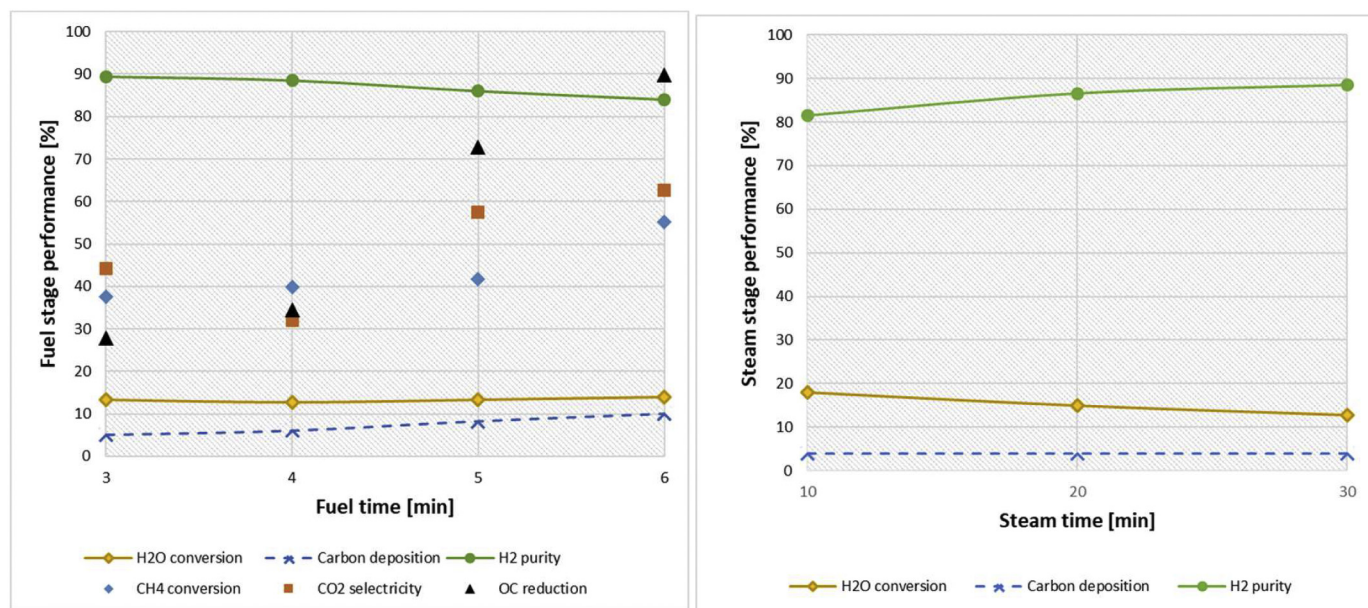


Fig. 16. The reactor performance at the fuel and steam stages at 800 °C and 1 bar. a) The performance at the fuel stage against fuel time at a constant steam time (5mins). b) The performance at the steam stage against steam time at constant fuel time (4mins).

Regarding carbon deposition, Fig. 15 clearly shows the formation of CO and CO₂ in the steam stage due to the gasification of deposited carbon by steam. It is shown that the concentration of CO₂ was significantly higher than that of CO, suggesting that the oxygen carrier catalyzes the water-gas shift reaction, which converts CO and excess steam to CO₂ and H₂. These released carbon-containing gases will reduce the CO₂ capture efficiency if the resulting H₂-rich stream is combusted for heat or power production.

Fig. 16 summarizes the reduction performance of the oxygen carrier as a function of the fuel and steam times. In these cases, data was extracted from a stage before significant agglomeration started, but it is possible that some initial agglomeration behavior already caused the reactor to exhibit some plug-flow behavior in these cases, thus increasing fuel conversion due to increased gas contact and residence time. Looking at the effect of fuel time (Fig. 16 a), higher H₂ yield was achieved with fuel times of 5 and 6 min (evident from H₂O conversion), but associated with higher carbon deposition and less H₂ purity as opposed to the fuel times of 3 and 4 min. At lower fuel time, the degree of fuel utilization with methane conversion (40%) mostly occurring through partial oxidation to syngas instead of full oxidation (CO₂ selectivity was in the range of 30–45%). Steam conversion of about 13% was obtained for all cases; more than 50% lower than the Fe₃O₄-FeO equilibrium at 800 °C. Carbon deposition at the fuel stage resulted in about 6% of the incoming carbon to end up in the H₂-rich stream from the steam stage. On a dry basis, these carbon-containing gases will reduce the H₂ purity to about 90%. At shorter steam stage (Fig. 16 b), higher steam conversion to H₂ was achieved but also with lower H₂ purity due to more of CO₂ and CO mixed into the released H₂. As shown in Fig. 15, H₂O conversion, through the gasification of the deposited carbon and water-gas-shift reaction are higher at the start of the steam stage, explaining these trends.

4. Conclusion

Two GSWS experimental campaigns were completed using 35 wt% Fe₂O₃ on Al₂O₃ and Cu-doped Fe/MgAl₂O₄ spinel of high iron content developed specifically in this study. The 1st GSWS demonstration was completed with 35 wt% Fe₂O₃ on Al₂O₃ OC in 5 cm ID fluidized bed reactor. Good reactor performance was achieved with no agglomeration

but H₂ purity was compromised due to gas mixing while switching between reactor stages. To improve H₂ purity, a mass balance calculation showed that up to 70 wt% iron content oxygen carrier is desired to keep the GSWS stages sufficiently long to minimize gas mixing effect on GSWS gas separation performance. On this ground, an optimized Cu-doped Mg(Fe_{0.9}Al_{0.1})₂O₄ spinel OC with 74 wt% active content was developed, screened and characterized using TGA, XRD, ICP-OES, SEM, ICP and crushing test for the 2nd GSWS demonstration in the 5 cm ID fluidized bed reactor. High oxygen-carrying capacity up to 20% was achieved and TGA result at 850 °C shows that the oxygen carrier is very reactive and exhibited good redox behavior.

However, the 2nd GSWS demonstration with the optimized Cu-doped Mg(Fe_{0.9}Al_{0.1})₂O₄ spinel OC with 74 wt% active content revealed three key challenges with the proposed high active content. All three of these challenges need to be addressed in future work to increase the attractiveness of the GSWS concept. Firstly, the degree of fuel utilization in the fuel stage was low, resulting in high fuel slipage. Such slipped fuel can be productively integrated with a downstream process, but it will certainly increase the attractiveness of the GSWS concept if fuel slip can be minimized. Secondly, the oxygen carrier started to agglomerate after about 34% of reduction. This issue does not allow the process to utilize even half of the oxygen-carrying capacity and will seriously hamper the CO₂ separation performance of the process. It is possible that this challenge can be overcome in a larger reactor where more vigorous fluidization is possible, but this needs to be confirmed in future experiments. Thirdly, the oxygen carrier showed significant carbon deposition, resulting in CO₂ and CO being released in the steam stage. When the H₂-rich stream is combusted, this will result in CO₂ emissions of about 20 kg/GJ_{LHV} of H₂. Alternatively, a downstream pressure swing adsorption unit can be used to purify the H₂ before utilization. The results from TGA appeared as if coking was delayed until 85% lattice oxygen conversion was achieved. This was possible because the rate of reduction was much faster in TGA than the rate of coking so that the net effect was mass loss even though coking occurred. This shows that TGA alone is not suitable to relate conversion with onset of coking.

To summarize, the following points could be noted:

- Gas Switching water-splitting could be an efficient technique for H₂ production with zero-emission.

- Oxygen carrier with 35 wt% active content performed well but with less H₂ purity without agglomeration, while the oxygen carrier with 74 wt% active content tends to agglomerate faster.
- A compromise in the active content is therefore required to achieve an optimum GSWs performance.
- Relying on a TGA alone is not so sufficient as many other factors, such as coking, agglomeration, could differ with large-scale setup.

Declaration of Competing Interest

The authors declare that they have no known competing financial interests or personal relationships that could have appeared to influence the work reported in this paper.

Acknowledgment

ACT GaSTech project. Project No 271511.

This project has received funding from The Research Council of Norway and is cofounded by the European Commission under the Horizon 2020 program, ACT Grant Agreement No 691712. This project also received the 2019 Publication Grant from Equinor. VATL Lab technicians at the Norwegian University of Science and Technology are equally acknowledged for constructing and maintaining the experimental setup.

Appendix A. Supplementary data

Supplementary data to this article can be found online at <https://doi.org/10.1016/j.powtec.2020.05.039>.

References

- [1] C. Ieaghe, Migration in the overburden, IEAGHG Technical Reports, 2017.
- [2] IPCC, Global Warming of 1.5C- An IPCC Special Report on the impacts of global warming of 1.5C above pre-industrial levels and related global greenhouse gas emission pathways, in the context of strengthening the global response to the threat of climate change, sustainable development, and efforts to eradicate poverty, Summary for Policymakers, IPCC, Switzerland, 2018.
- [3] F. He, F. Li, Perovskite promoted iron oxide for hybrid water-splitting and syngas generation with exceptional conversion, *Energy Environ. Sci.* 8 (2) (2015) 535–539.
- [4] P. Nejat, et al., A global review of energy consumption, CO₂ emissions and policy in the residential sector (with an overview of the top ten CO₂ emitting countries), *Renew. Sust. Energ. Rev.* 43 (2015) 843–862.
- [5] J. Cook, et al., Quantifying the consensus on anthropogenic global warming in the scientific literature, *Environ. Res. Lett.* 8 (2) (2013), 024024.
- [6] R.K. Pachauri, et al., Climate Change 2014: Synthesis Report. Contribution of Working Groups I, II and III to the Fifth Assessment Report of the Intergovernmental Panel on Climate Change, IPCC, 2014.
- [7] N. U. Adoption of the Paris Agreement Proposal by the President, [cited 2018 May]; Available from: <https://unfccc.int/resource/docs/2015/cop21/eng/l09r01.pdf> 2015.
- [8] C.C. Elam, et al., Realizing the hydrogen future: the International Energy Agency's efforts to advance hydrogen energy technologies, *Int. J. Hydrog. Energy* 28 (6) (2003) 601–607.
- [9] G. Voitic, V. Hacker, Recent advancements in chemical looping water splitting for the production of hydrogen, *RSC Adv.* 6 (100) (2016) 98267–98296.
- [10] P.P. Edwards, et al., Hydrogen and fuel cells: towards a sustainable energy future, *Energy Policy* 36 (12) (2008) 4356–4362.
- [11] J.D. Holladay, et al., An overview of hydrogen production technologies, *Catal. Today* 139 (4) (2009) 244–260.
- [12] J. Adanez, et al., Progress in chemical-looping combustion and reforming technologies, *Prog. Energy Combust. Sci.* 38 (2) (2012) 215–282.
- [13] S.K. Ngoh, D. Njomo, An overview of hydrogen gas production from solar energy, *Renew. Sust. Energ. Rev.* 16 (9) (2012) 6782–6792.
- [14] R. Chaubey, et al., A review on development of industrial processes and emerging techniques for production of hydrogen from renewable and sustainable sources, *Renew. Sust. Energ. Rev.* 23 (2013) 443–462.
- [15] E.J. Anthony, Solid looping cycles: a new technology for coal conversion, *Ind. Eng. Chem. Res.* 47 (6) (2008) 1747–1754.
- [16] M. Rydén, M. Arjmand, Continuous hydrogen production via the steam-iron reaction by chemical looping in a circulating fluidized-bed reactor, *Int. J. Hydrog. Energy* 37 (6) (2012) 4843–4854.
- [17] T.-L. Hsieh, et al., 250 kWth high pressure pilot demonstration of the syngas chemical looping system for high purity H₂ production with CO₂ capture, *Appl. Energy* 230 (2018) 1660–1672.
- [18] M.N. Khan, T. Shamim, Investigation of hydrogen generation in a three reactor chemical looping reforming process, *Appl. Energy* 162 (2016) 1186–1194.
- [19] M.N. Khan, T. Shamim, Exergoeconomic analysis of a chemical looping reforming plant for hydrogen production, *Int. J. Hydrog. Energy* 42 (8) (2017) 4951–4965.
- [20] M.V. Kathe, et al., Hydrogen production from natural gas using an iron-based chemical looping technology: thermodynamic simulations and process system analysis, *Appl. Energy* 165 (2016) 183–201.
- [21] Lane, H., Apparatus for producing hydrogen gas. 1912, Google Patents.
- [22] L.-S. Fan, F. Li, Chemical looping technology and its fossil energy conversion applications, *Ind. Eng. Chem. Res.* 49 (21) (2010) 10200–10211.
- [23] T. Proell, et al., Syngas and a separate nitrogen/argon stream via chemical looping reforming - a 140 kW pilot plant study, *Fuel* 89 (6) (2010) 1249–1256.
- [24] B. Kronberger, et al., A two-compartment fluidized bed reactor for CO₂ capture by chemical-looping combustion, *Chem. Eng. Technol.* 27 (12) (2004) 1318–1326.
- [25] C. Linderholm, et al., 160 h of chemical-looping combustion in a 10 kW reactor system with a NiO-based oxygen carrier, *Int. J. Greenh. Gas Control* 2 (4) (2008) 520–530.
- [26] E. Johansson, et al., A 300 W laboratory reactor system for chemical-looping combustion with particle circulation, *Fuel* 85 (10–11) (2006) 1428–1438.
- [27] N. Ding, et al., Development and testing of an interconnected fluidized-bed system for chemical looping combustion, *Chem. Eng. Technol.* 35 (3) (2012) 532–538.
- [28] P. Kolbitsch, et al., Operating experience with chemical looping combustion in a 120 kW dual circulating fluidized bed (DCFB) unit, *Int. J. Greenh. Gas Control* 4 (2) (2010) 180–185.
- [29] M. Rydén, A. Lyngfelt, Using steam reforming to produce hydrogen with carbon dioxide capture by chemical-looping combustion, *Int. J. Hydrog. Energy* 31 (10) (2006) 1271–1283.
- [30] M. Rydén, A. Lyngfelt, T. Mattisson, Synthesis gas generation by chemical-looping reforming in a continuously operating laboratory reactor, *Fuel* 85 (12–13) (2006) 1631–1641.
- [31] L.F. de Diego, et al., Hydrogen production by chemical-looping reforming in a circulating fluidized bed reactor using Ni-based oxygen carriers, *J. Power Sources* 192 (1) (2009) 27–34.
- [32] M. Luo, et al., Review of hydrogen production using chemical-looping technology, *Renew. Sust. Energ. Rev.* 81 (2018) 3186–3214.
- [33] H.P. Hamers, et al., Comparison on process efficiency for CLC of syngas operated in packed bed and fluidized bed reactors, *Int. J. Greenh. Gas Control* 28 (0) (2014) 65–78.
- [34] R. Xiao, et al., Pressurized chemical-looping combustion of coal using an iron ore as oxygen carrier in a pilot-scale unit, *Int. J. Greenh. Gas Control* 10 (2012) 363–373.
- [35] L. Chen, et al., Pressurized chemical looping combustion for solid fuel, *Handbook of Chemical Looping Technology* (2018) 123–158.
- [36] S. Zhang, R. Xiao, W. Zheng, Comparative study between fluidized-bed and fixed-bed operation modes in pressurized chemical looping combustion of coal, *Appl. Energy* 130 (2014) 181–189.
- [37] A. Bischi, et al., Design study of a 150 kWth double loop circulating fluidized bed reactor system for chemical looping combustion with focus on industrial applicability and pressurization, *Int. J. Greenh. Gas Control* 5 (3) (2011) 467–474.
- [38] J. Adanez, et al., Progress in chemical-looping combustion and reforming technologies, *Prog. Energy Combust. Sci.* 38 (2) (2012) 215–282.
- [39] N.M.F. Science, Chemical Looping Combustion, [cited 2019 June]; Available from: <https://mfix.netl.doe.gov/research/chemical-looping-combustion/>.
- [40] A. Zaabout, et al., Experimental demonstration of a novel gas switching combustion reactor for power production with integrated CO₂ capture, *Ind. Eng. Chem. Res.* 52 (39) (2013) 14241–14250.
- [41] S. Noorman, M. van Sint Annaland, H. Kuipers, Packed bed reactor technology for chemical-looping combustion, *Ind. Eng. Chem. Res.* 46 (12) (2007) 4212–4220.
- [42] H. Hamers, et al., A novel reactor configuration for packed bed chemical-looping combustion of syngas, *Int. J. Greenh. Gas Control* 16 (2013) 1–12.
- [43] A. Ugwu, et al., Gas switching reforming for syngas production with iron-based oxygen carrier-the performance under pressurized conditions, *Int. J. Hydrog. Energy* 45 (2) (2020) 1267–1282.
- [44] A. Zaabout, et al., Gas switching reforming (GSR) for syngas production with integrated CO₂ capture using iron-based oxygen carriers, *Int. J. Greenh. Gas Control* 81 (2019) 170–180.
- [45] S.M. Nazir, et al., Gas switching reforming (GSR) for power generation with CO₂ capture: process efficiency improvement studies, *Energy* 167 (2019) 757–765.
- [46] S.M. Nazir, et al., Efficient hydrogen production with CO₂ capture using gas switching reforming, *Energy* 185 (2019) 372–385.
- [47] A. Ugwu, A. Zaabout, S. Amini, An advancement in CO₂ utilization through novel gas switching dry reforming, *Int. J. Greenh. Gas Control* 90 (2019) 102791.
- [48] M. Osman, et al., Internally circulating fluidized-bed reactor for syngas production using chemical looping reforming, *Chem. Eng. J.* 377 (2018) 120076.
- [49] S.A. Wassie, et al., Hydrogen production with integrated CO₂ capture in a novel gas switching reforming reactor: proof-of-concept, *Int. J. Hydrog. Energy* 42 (21) (2017) 14367–14379.
- [50] S.A. Wassie, et al., Hydrogen production with integrated CO₂ capture in a membrane assisted gas switching reforming reactor: proof-of-concept, *Int. J. Hydrog. Energy* 43 (12) (2018) 6177–6190.
- [51] A. Zaabout, S. Cloete, S. Amini, Autothermal operation of a pressurized gas switching combustion with ilmenite ore, *Int. J. Greenh. Gas Control* 63 (2017) 175–183.
- [52] A. Zaabout, et al., Experimental demonstration of a novel gas switching combustion reactor for power production with integrated CO₂ capture, *Ind. Eng. Chem. Res.* 52 (39) (2013) 14241–14250.
- [53] S.M. Nazir, et al., Techno-economic assessment of the novel gas switching reforming (GSR) concept for gas-fired power production with integrated CO₂ capture, *Int. J. Hydrog. Energy* 43 (18) (2018) 8754–8769.

- [54] S. Szima, et al., Gas switching reforming for flexible power and hydrogen production to balance variable renewables, *Renew. Sust. Energ. Rev.* 110 (2019) 207–219.
- [55] P. Chiesa, et al., Three-reactors chemical looping process for hydrogen production, 33 (9) (2008) 2233–2245.
- [56] P. Chiesa, et al., Three-reactors chemical looping process for hydrogen production, *Int. J. Hydrog. Energy* 33 (9) (2008) 2233–2245.
- [57] C.E. Agu, et al., Investigation of bubbling behaviour in deep fluidized beds at different gas velocities using electrical capacitance tomography, 2019.
- [58] C.E. Agu, et al., Determination of onset of bubbling and slugging in a fluidized bed using a dual-plane electrical capacitance tomography system, 328, 2017 997–1008.
- [59] J.C. Abanades, et al., Fluidized bed combustion systems integrating CO₂ capture with CaO, 2005 2861–2866 39(8).
- [60] A. Zaabout, et al., A novel gas switching combustion reactor for power production with integrated CO₂ capture: sensitivity to the fuel and oxygen carrier types, *Int. J. Greenh. Gas Control* 39 (2015) 185–193.
- [61] S.A. Wassie, et al., Hydrogen production with integrated CO₂ capture in a novel gas switching reforming reactor: proof-of-concept, 42 (21) (2017) 14367–14379.
- [62] S. Cloete, et al., Integration of a gas switching combustion (GSC) system in integrated gasification combined cycles, *Int. J. Greenh. Gas Control* 42 (2015) 340–356.
- [63] C.A. del Pozo, et al., The potential of chemical looping combustion using the gas switching concept to eliminate the energy penalty of CO₂ capture, *Int. J. Greenh. Gas Control* 83 (2019) 265–281.
- [64] K. Svoboda, et al., Thermodynamic possibilities and constraints for pure hydrogen production by iron based chemical looping process at lower temperatures, *Energy Convers. Manag.* 48 (12) (2007) 3063–3073.
- [65] N. Saithong, et al., Thermodynamic analysis of the novel chemical looping process for two-grade hydrogen production with CO₂ capture, *Energy Convers. Manag.* 180 (2019) 325–337.
- [66] Y. De Vos, et al., Processing and characterization of Fe-based oxygen carriers for chemical looping for hydrogen production, *Int. J. Greenh. Gas Control* 70 (2018) 12–21.
- [67] H. Chen, et al., Reduction of hematite (Fe₂O₃) to metallic iron (Fe) by CO in a micro fluidized bed reaction analyzer: a multistep kinetics study, *Powder Technol.* 316 (2017) 410–420.
- [68] D. Kang, et al., Syngas production on a Ni-enhanced Fe₂O₃/Al₂O₃ oxygen carrier via chemical looping partial oxidation with dry reforming of methane, *Appl. Energy* 211 (2018) 174–186.
- [69] L. Protasova, F. Snijkers, Recent developments in oxygen carrier materials for hydrogen production via chemical looping processes, *Fuel* 181 (2016) 75–93.
- [70] F. Li, et al., Ionic diffusion in the oxidation of iron—effect of support and its implications to chemical looping applications, *Energy Environ. Sci.* 4 (3) (2011) 876–880.
- [71] D. Sanfilippo, One-step hydrogen through water splitting with intrinsic CO₂ capture in chemical looping, *Catal. Today* 272 (2016) 58–68.
- [72] W. Liu, et al., Inhibiting the interaction between FeO and Al₂O₃ during chemical looping production of hydrogen, *RSC Adv.* 5 (3) (2015) 1759–1771.
- [73] R.D. Solunke, G.T. Veser, Hydrogen production via chemical looping steam reforming in a periodically operated fixed-bed reactor, *Ind. Eng. Chem. Res.* 49 (21) (2010) 11037–11044.
- [74] Q. Imtiaz, et al., Development of MgAl₂O₄-stabilized, Cu-doped, Fe₂O₃-based oxygen carriers for thermochemical water-splitting, *J. Mater. Chem. A* 4 (1) (2016) 113–123.
- [75] J.Y. Do, et al., Reliable oxygen transfer in MgAl₂O₄ spinel through the reversible formation of oxygen vacancies by Cu²⁺/Fe³⁺ anchoring, *Appl. Energy* 219 (2018) 138–150.
- [76] D. Hosseini, et al., Reversible exsolution of dopant improves the performance of Ca₂Fe₂O₅ for chemical looping hydrogen production, *ACS Appl. Mater. Interfaces* 11 (20) (2019) 18276–18284.
- [77] C. Chung, et al., Chemically and physically robust, commercially-viable iron-based composite oxygen carriers sustainable over 3000 redox cycles at high temperatures for chemical looping applications, *Energy Environ. Sci.* 10 (11) (2017) 2318–2323.